



# Zwicky Transient Facility and Globular Clusters: The RR Lyrae *gri*-band Period–Luminosity–Metallicity and Period–Wesenheit–Metallicity Relations

Chow-Choong Ngeow<sup>1</sup> , Anupam Bhardwaj<sup>2,3</sup> , Richard Dekany<sup>4</sup> , Dmitry A. Duev<sup>5</sup> , Matthew J. Graham<sup>5</sup> , Steven L. Groom<sup>6</sup> , Ashish A. Mahabal<sup>5,7</sup> , Frank J. Masci<sup>6</sup> , Michael S. Medford<sup>8,9</sup> , and Reed Riddle<sup>4</sup>

<sup>1</sup> Graduate Institute of Astronomy, National Central University, 300 Jhongda Road, 32001 Jhongli, Taiwan; [cngeow@astro.ncu.edu.tw](mailto:cngeow@astro.ncu.edu.tw)

<sup>2</sup> Korea Astronomy and Space Science Institute, Daedeokdae-ro 776, Yuseong-gu, Daejeon 34055, Republic of Korea

<sup>3</sup> INAF–Osservatorio astronomico di Capodimonte, Via Moiariello 16, 80131 Napoli, Italy

<sup>4</sup> Caltech Optical Observatories, California Institute of Technology, Pasadena, CA 91125, USA

<sup>5</sup> Division of Physics, Mathematics, and Astronomy, California Institute of Technology, Pasadena, CA 91125, USA

<sup>6</sup> IPAC, California Institute of Technology, 1200 E. California Boulevard, Pasadena, CA 91125, USA

<sup>7</sup> Center for Data Driven Discovery, California Institute of Technology, Pasadena, CA 91125, USA

<sup>8</sup> University of California, Berkeley, Department of Astronomy, Berkeley, CA 94720, USA

<sup>9</sup> Lawrence Berkeley National Laboratory, 1 Cyclotron Road, Berkeley, CA 94720, USA

Received 2022 January 29; revised 2022 March 24; accepted 2022 March 25; published 2022 April 28

## Abstract

Based on time-series observations collected from the Zwicky Transient Facility (ZTF), we derived period–luminosity–metallicity (PLZ) and period–Wesenheit–metallicity (PWZ) relations for RR Lyrae located in globular clusters. We have applied various selection criteria to exclude RR Lyrae with problematic or spurious light curves. These selection criteria utilized information on the number of data points per light curve, amplitudes, colors, and residuals on the period–luminosity and/or period–Wesenheit relations. Due to blending, a number of RR Lyrae in globular clusters were found to be anomalously bright and have small amplitudes of their ZTF light curves. We used our final sample of  $\sim 750$  RR Lyrae in 46 globular clusters covering a wide metallicity range ( $-2.36 \text{ dex} < [\text{Fe}/\text{H}] < -0.54 \text{ dex}$ ) to derive PLZ and PWZ relations in the *gri* bands. In addition, we have also derived the period–color–metallicity and, for the first time, the period–*Q*-index–metallicity relations, where the *Q*-index is extinction-free by construction. We have compared our various relations to empirical and theoretical relations available in the literature and found a good agreement with most studies. Finally, we applied our derived PLZ relation to a dwarf galaxy, Crater II, and found that its true distance modulus should be larger than the most recent determination.

*Unified Astronomy Thesaurus concepts:* Globular star clusters (656); RR Lyrae variable stars (1410); Distance indicators (394); Wide-field telescopes (1800); Sky surveys (1464)

*Supporting material:* machine-readable table

## 1. Introduction

The RR Lyrae variables are exclusively old ( $\gtrsim 10$  Gyr), low-mass, short-period pulsating stars that are well-known standard candles with numerous applications in astrophysics. This is because RR Lyrae exhibit the period–luminosity–metallicity (PLZ) relations that can be used to determine distance, where metallicity is approximated by  $[\text{Fe}/\text{H}]$ . In the *V* band, the slope of the PLZ relation almost vanishes due to a nearly flat bolometric correction for a range of temperatures within the instability strip of RR Lyrae (Bono 2003; Bono et al. 2003), leaving an absolute *V*-band magnitude and metallicity,  $M_V - [\text{Fe}/\text{H}]$ , relation. Toward the near-infrared *K* band, the bolometric correction is a linear function of temperature, hence exhibiting a PLZ relation (Bono et al. 2001, 2003; Bono 2003; Marconi et al. 2003). Indeed, RR Lyrae exhibit PLZ relations in *R*-band and longer wavelengths, as demonstrated, for example, in Catelan et al. (2004), Marconi et al. (2015), and Neeley et al. (2017, 2019). A wealth of literature can be found on the calibrations of the  $M_V - [\text{Fe}/\text{H}]$  and/or PLZ relations (especially in the *K* band), for example, the reviews presented in Smith

(2004), Sandage & Tammann (2006), Bono et al. (2016), Beaton et al. (2018), and Bhardwaj (2020, 2022), and references therein.

In optical bands, the PLZ relations, especially the  $M_V - [\text{Fe}/\text{H}]$  relation,<sup>10</sup> are well established in the Johnson–Cousins (*BVR*) filters and were recently extended to the Gaia *G* band (Muraveva et al. 2018). In contrast, there are only a few empirical calibrations of the PLZ relations in the Sloan or Sloan-like filters. Based on the Pan-STARRS1 data for  $\sim 50$  RR Lyrae in five globular clusters, Sesar et al. (2017) derived the empirical *griz* PLZ relations. Vivas et al. (2017) calibrated *ugriz* period–luminosity (PL) relations for both fundamental mode ab-type and first-overtone c-type RR Lyrae (or RRab and RRc, respectively) in M5 with Dark Energy Camera (DECam; Flaugher et al. 2015) observations. Recently, Bhardwaj et al. (2021) derived the *gi*-band (and *JK<sub>s</sub>*-band) PL relations for both types of RR Lyrae in M15 using archival Canada–France–Hawaii Telescope data. These works were either based on a particular globular cluster or relied on a rather limited sample of globular clusters that host RR Lyrae. For a comparison, Sollima et al. (2006) demonstrated that a *K*-band PLZ relation can be derived from a sample of 538 RR Lyrae in 16 globular clusters. Similarly, Dambis et al. (2014) derived the PLZ relations in the mid-infrared W1 and W2 bands using a sample

Original content from this work may be used under the terms of the [Creative Commons Attribution 4.0 licence](https://creativecommons.org/licenses/by/4.0/). Any further distribution of this work must maintain attribution to the author(s) and the title of the work, journal citation and DOI.

<sup>10</sup> We recall that the  $M_V - [\text{Fe}/\text{H}]$  relation is a special case of PLZ relation with vanishing slope.

**Table 1**  
Comparison of Optical Time-domain Surveys in the Northern Sky

Survey <sup>a</sup>	Filters <sup>b</sup>	Pixel Scale <sup>c</sup>	Photometry <sup>d</sup>	Depth
ZTF	<i>gri</i>	1.01	PSF and AP	$r \sim 20.6$
PS1 $3\pi$	<i>grizy</i>	0.258	PSF and AP	$r \sim 21.8$
ATLAS	<i>oc</i>	1.86	PSF	$m \sim 19.5$
ASAS-SN	<i>gV</i>	8.0	AP	$V \sim 17$
CSS	...	1.5	AP	$V \sim 19.5$
LINEAR	...	2.25	AP	$m \sim 18$
SuperWASP	...	13.7	AP	$V \sim 15$

#### Notes.

<sup>a</sup> Abbreviation for each survey (references are the sources of information entering into this table): ZTF = Zwicky Transient Facility (Bellm et al. 2019; Masci et al. 2019); PS1  $3\pi$  = Pan-STARRS1  $3\pi$  Survey (Chambers et al. 2016; Magnier et al. 2020; see also <https://panstarrs.stsci.edu/>); ATLAS = Asteroid Terrestrial-impact Last Alert System (Heinze et al. 2018; Tonry et al. 2018); ASAS-SN = All-Sky Automated Survey for Supernovae (Kochanek et al. 2017); CSS = Catalina Schmidt Survey (Drake et al. 2013; see also <https://catalina.lpl.arizona.edu/>); LINEAR = Lincoln Near-Earth Asteroid Research (Sesar et al. 2011); SuperWASP = Super Wide Angle Search for Planets (Pollacco et al. 2006).

<sup>b</sup> For simplicity, we refer to the variants of the Sloan-like filters as *ugriz*; for example, the ZTF filters are *gri* instead of  $g_{ZTF}$ ,  $r_{ZTF}$ , and  $i_{ZTF}$ . An ellipse means no filter or a clear filter.

<sup>c</sup> In units of arcseconds per pixel.

<sup>d</sup> AP = aperture photometry.

of 360 RR Lyrae in 15 globular clusters and 275 RR Lyrae in nine globular clusters, respectively. Finally, Nemec et al. (1994) derived the BVK-band PLZ relations using more than 1000 RR Lyrae in 22 globular clusters (with  $\sim 195$ –552 RR Lyrae, depending on the filters), the Magellanic Clouds, and five local dwarf galaxies.

Hence, the purpose of this work is to use a large number of globular clusters observed by the Zwicky Transient Facility (ZTF; Bellm & Kulkarni 2017) to improve the derivation of RR Lyrae PLZ relations in Sloan-like filters. In addition to PLZ relations, we also derive the period–Wesenheit–metallicity (PWZ) relation using the same data set because the Wesenheit magnitudes are, by construction, extinction-free (Madore 1982; Madore & Freedman 1991). Table 1 compares a number of representative time-domain surveys that cover a similar part of the northern sky as observed by ZTF. Given that our target RR Lyrae are located in globular clusters, surveys with large pixel scales and/or catalog products based on aperture photometry are not suitable for our purpose. Time-series data from ATLAS offer competitive quality and quantities similar to ZTF; however, the main observations of ATLAS were conducted in the customized *o* and *c* filters. The PS1  $3\pi$  Survey has a smaller pixel scale and can reach a deeper depth than ZTF, but the typical number of observations in each filter is  $\lesssim 12$  over its  $\sim 4.5$  yr of operation (Sesar et al. 2017). In contrast, the average number of ZTF observations on our target globular clusters are  $\sim 218$ ,  $\sim 334$ , and  $\sim 95$  in the *gri* bands, respectively (see Section 2). The homogeneous and unique ZTF data provide several advantages over other time-domain imaging surveys for our purposes, such as observations done in the *gri* filters and with a fine pixel scale, the availability of catalogs based on the point-spread function (PSF) photometry, a competitive depth to reach most of the globular clusters in the northern sky, and numerous observations over a period of  $\sim 4$  yr.

Section 2 describes our sample of RR Lyrae in globular clusters, their ZTF light-curve data, and the light-curve fittings

to derive their mean magnitudes. We further filtered out RR Lyrae with problematic light curves using information on the amplitudes, colors, and residuals of the PL and period–Wesenheit (PW) relations in Section 3. The PLZ and PWZ relations were then derived in Section 4 based on the final sample. As by-products, we also derived the period–color–metallicity (PCZ) relations and investigated the color–color diagram in Section 5. As an example of application, we derived the distance to a dwarf galaxy, Crater II, using published data together with our derived PLZ relations in Section 6, followed by conclusions given in Section 7.

## 2. Sample and Data

### 2.1. Selections of Globular Clusters and RR Lyrae

The Updated Catalog of Variable Stars in Globular Clusters (Clement et al. 2001; Clement 2017, hereafter Clement’s Catalog) was used to select RR Lyrae in globular clusters. We first selected globular clusters that are visible from the Palomar Observatory (i.e., decl.  $> -30^\circ$ ) and contain at least one RR Lyrae, either type RR0 (aka RRab, or fundamental mode) or RR1 (aka RRc, or first-overtone mode). The foreground or suspected foreground RR Lyrae labeled in Clement’s Catalog, however, were not included in our selection. We further removed four duplicated entries in M80 from Clement’s Catalog, as well as three close “pairs” of (blended) RR Lyrae in M3 (4n/s, 250n/s, and 270n/s; see Guhathakurta et al. 1994; Chicherov 1997; Corwin & Carney 2001; Benkó et al. 2006), because they cannot be separated from ZTF observations. Therefore, our initial list contains 961 RR0 and 543 RR1,<sup>11</sup> for a total of 1504 RR Lyrae, in 57 globular clusters.

### 2.2. Adopted Distances, Reddenings, and Metallicity

Homogeneous distances to the selected globular clusters were adopted from the latest compilation given in Baumgardt & Vasiliev (2021).<sup>12</sup> Based on the adopted globular cluster distances, the reddening  $E$  toward each of the RR Lyrae was obtained using the Bayerstar2019 3D reddening map<sup>13</sup> (Green et al. 2019) via *dustmaps*.<sup>14</sup> Finally, homogeneous values of [Fe/H] for these globular clusters were adopted from the GLOBular clusTer Homogeneous Abundances Measurements (GOTHAM) survey<sup>15</sup> (Dias et al. 2015, 2016a, 2016b; Vásquez et al. 2018).

### 2.3. ZTF Light-curve Extraction

The ZTF<sup>16</sup> is a dedicated time-domain wide-field synoptic sky survey aimed at exploring the transient universe. It utilizes the Palomar 48 inch Samuel Oschin Schmidt telescope together with a new mosaic CCD camera that provides a field of view of

<sup>11</sup> Note that the pulsation mode for V4 and V5 in 2MASS-GC02 should be RR1 (Borissova et al. 2007); however, they were mislabeled as RR0 in Clement’s Catalog. Similarly, V20 in M22 (Kunder et al. 2013) and V21 in M80 (Kopacki 2013) should be RR0; they were mislabeled as RR1 in Clement’s Catalog.

<sup>12</sup> <https://people.smp.uq.edu.au/HolgerBaumgardt/globular/orbits.html>

<sup>13</sup> <http://argonaut.skymaps.info/>

<sup>14</sup> <https://dustmaps.readthedocs.io/en/latest/> (Green 2018) python package.

<sup>15</sup> [http://www.sc.eso.org/~bdias/files/dias+16\\_MWGC.txt](http://www.sc.eso.org/~bdias/files/dias+16_MWGC.txt)

<sup>16</sup> Technically, ZTF includes two phases of operation due to a difference in funding profiles; before and after 2020 December 1 are known as ZTF-I and ZTF-II, respectively. For simplicity, we collectively refer to them as ZTF in this work.

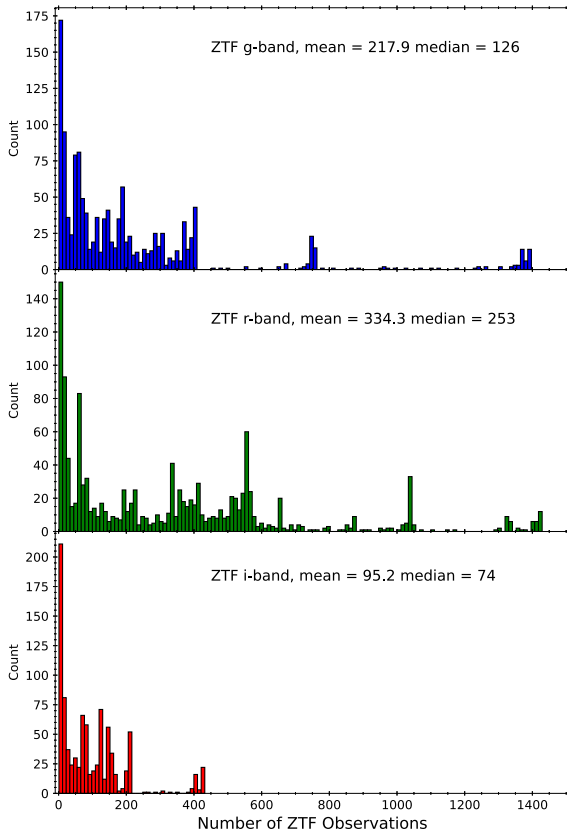


**Figure 1.** Histograms of the number of ZTF observations for our sample of RR Lyrae in the globular clusters. The mean and median numbers of observations are also given in the upper right corner of each panel.

47 deg<sup>2</sup> to observe the northern sky in customized *gri* filters. Observing time and the data right of ZTF was divided into three high-level surveys: partner surveys, public surveys, and California Institute of Technology (Caltech) surveys. Further details regarding ZTF can be found in Bellm et al. (2019), Graham et al. (2019), and Dekany et al. (2020) and will not be repeated here. Imaging data taken from ZTF were processed with a dedicated reduction pipeline, which is described in detail in Masci et al. (2019). The final ZTF data products included reduced images and catalogs based on both aperture and PSF photometry.

The ZTF *gri*-band light curves were extracted for our sample of RR Lyrae from the PSF catalogs available from both the ZTF Public Data Release 7<sup>17</sup> (including both public and Caltech data) and the partner surveys until 2021 September 30. Using a matching radius of 1", the *gri*-band light curves of 1329 RR Lyrae in our initial list, whenever available, were extracted. Distributions of the number of data points per light curve  $N$  (in the *gri* band separately) are presented in Figure 1, where  $N$  can be as large as  $\sim 1390$  in the *g* band. The number of data points in the *i*-band light curves is much smaller due to a combination of several things, such as the late arrival of the *i*-band filter, the ZTF public surveys being conducted in the *g* band only, and the observing strategies for ZTF partnership surveys being focused on the *g* band in the early time. Out of the 1329 RR Lyrae in our sample, 1328 of them have ZTF data in either the *g* or *r* band (or both), but only 907 RR Lyrae have ZTF observations in the *i* band.

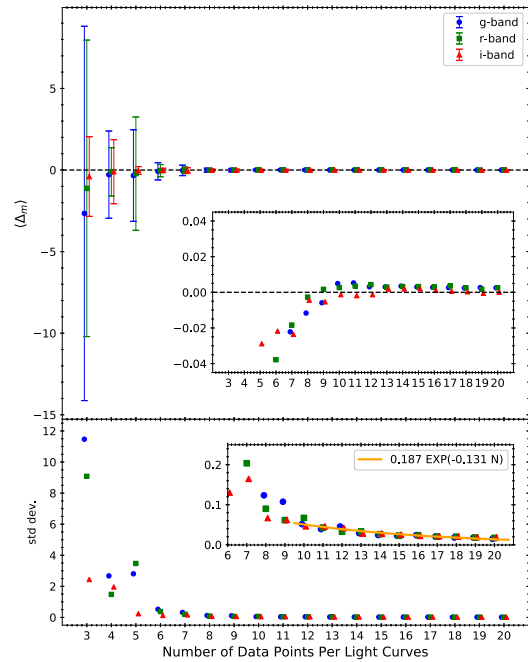


**Figure 2.** Results of error estimation based on simulated light curves (see text for details) for the mean magnitudes obtained with template light-curve fittings. For a better visualization, the *g*- and *i*-band data points were offset slightly on the  $x$ -axis. The upper panel presents the averaged  $\langle \Delta_m \rangle$  obtained from 1000 simulated light curves as a function of  $N$ , the number of data points per light curve. The error bars represent a  $1\sigma$  standard deviation on the averaged values. The horizontal dashed lines represent  $\langle \Delta_m \rangle = 0$ . The inset in the upper panel is an enlarged version with error bars omitted for clarity. In the lower panel, the corresponding standard deviations were plotted as a function of  $N$ . The orange curve in the inset is the best-fit exponential decay function to describe the trend of the standard deviations, at which the fittings of the exponential decay function were only done on data points with  $N \geq 10$ .

## 2.4. Light-curve Fittings

A template light-curve fitting approach was adopted to derive the mean magnitudes in the *gri* band for our sample of RR Lyrae. Since we do not have well-constrained amplitudes for the RR Lyrae in our sample, we solved for the amplitude, phase shift, and mean magnitude as free parameters. Given that the minimum number of data points per phased light curve to fit with a template light curve is three, to account for the scaling (i.e., amplitude), the  $x$ -shift (i.e., the phase shift), and the  $y$ -shift (i.e., the mean magnitude) of the light curves, we further restricted the fitting to be performed only on the ZTF light curve in any band that contains at least three data points. The `RRLyraeTemplateModelerMultiband` module available in the `astroML/gatspy`<sup>18</sup> package (hereafter `gatspy`; VanderPlas & Ivezić 2015) was employed to fit the ZTF light curves using the *gri*-band template light curves derived in Sesar et al. (2010). During the light-curve fitting, the periods of the RR Lyrae were also revised from the initial values given in Clement's Catalog, as improvements in the fitted light curves can be seen on these RR Lyrae.

By default, `gatspy` will fit a given light curve with both RR0 and RR1 template light curves. Since the pulsation types of our sample of RR Lyrae are known from Clement's Catalog, we modified the `gatspy` code to only use either the RR0 or RR1 template light curves for a given RR Lyrae. To remove dubious outliers in the light curves, we adopted a two-iteration

<sup>17</sup> <https://www.ztf.caltech.edu/page/dr7>

<sup>18</sup> <https://github.com/astroML/gatspy>; also see VanderPlas (2016).

**Table 2**  
List of Globular Clusters and the Number of RR Lyrae in the Sample

Globular Cluster	[Fe/H] (dex) <sup>a</sup>	$n_g^{\text{RR0}}$	$n_r^{\text{RR0}}$	$n_i^{\text{RR0}}$	$n_g^{\text{RR1}}$	$n_r^{\text{RR1}}$	$n_i^{\text{RR1}}$	$n_{\text{tot}}^{\text{b}}$	$D$ (kpc) <sup>a</sup>	$\langle E \rangle^{\text{c}}$
NGC 6426	-2.36 ± 0.03	7	7	0	5	5	0	12	20.71 ± 0.35	0.366
M30	-2.33 ± 0.03	3	4	0	2	2	0	6	8.46 ± 0.09	0.000
M15	-2.27 ± 0.01	53	50	47	53	48	39	109	10.71 ± 0.10	0.141
M92	-2.27 ± 0.06	11	10	10	6	6	6	17	8.50 ± 0.07	0.000
M68	-2.25 ± 0.02	14	14	0	16	16	0	30	10.40 ± 0.10	0.084
NGC 5053	-2.24 ± 0.16	6	6	5	4	4	4	10	17.54 ± 0.23	0.001
NGC 2419	-2.12 ± 0.16	26	27	18	30	30	15	57	88.47 ± 2.40	0.134
NGC 5897	-1.99 ± 0.03	3	3	0	3	3	0	6	12.55 ± 0.24	0.089
NGC 4147	-1.95 ± 0.09	5	5	5	10	10	10	15	18.54 ± 0.21	0.000
M22	-1.92 ± 0.02	10	10	0	13	14	0	24	3.30 ± 0.04	0.356
NGC 6293	-1.92 ± 0.10	2	2	0	2	2	0	4	9.19 ± 0.28	0.410
M53	-1.90 ± 0.05	29	29	28	29	30	28	59	18.50 ± 0.18	0.004
Palomar 13	-1.85 ± 0.16	4	4	4	0	0	0	4	23.48 ± 0.40	0.109
NGC 5466	-1.82 ± 0.08	12	13	13	7	7	7	20	16.12 ± 0.16	0.005
M56	-1.80 ± 0.15	1	1	1	2	2	2	3	10.43 ± 0.14	0.191
NGC 5634	-1.77 ± 0.04	8	9	7	6	6	6	15	25.96 ± 0.62	0.073
M80	-1.72 ± 0.04	6	5	0	6	6	0	12	10.34 ± 0.12	0.210
M19	-1.70 ± 0.05	1	1	0	0	0	0	1	8.34 ± 0.16	0.330
M9	-1.70 ± 0.08	7	7	0	8	8	0	15	8.30 ± 0.14	0.373
NGC 7492	-1.67 ± 0.12	1	1	1	2	2	2	3	24.39 ± 0.57	0.029
Palomar 3	-1.60 ± 0.16	6	6	3	0	0	0	6	94.84 ± 3.23	0.004
M79	-1.57 ± 0.02	5	5	0	3	3	0	8	13.08 ± 0.18	0.009
NGC 7006	-1.57 ± 0.05	48	41	39	4	3	2	53	39.32 ± 0.56	0.136
M13	-1.55 ± 0.05	1	1	1	8	7	6	9	7.42 ± 0.08	0.000
M2	-1.51 ± 0.02	21	21	15	10	11	8	32	11.69 ± 0.11	0.016
M3	-1.48 ± 0.05	101	132	88	24	35	18	167	10.18 ± 0.08	0.035
NGC 6934	-1.48 ± 0.11	61	62	55	8	8	7	72	15.72 ± 0.17	0.098
NGC 6355	-1.46 ± 0.06	4	4	0	1	1	0	5	8.65 ± 0.22	0.865
Palomar 5	-1.38 ± 0.16	0	0	0	5	5	0	5	21.94 ± 0.51	0.086
NGC 6235	-1.37 ± 0.08	1	2	0	1	1	0	3	11.94 ± 0.38	0.379
M72	-1.35 ± 0.08	34	35	0	6	6	0	41	16.66 ± 0.18	0.041
NGC 6229	-1.35 ± 0.16	40	36	33	15	15	15	55	30.11 ± 0.47	0.096
NGC 288	-1.33 ± 0.03	1	1	1	1	1	0	2	8.99 ± 0.09	0.015
M14	-1.28 ± 0.07	4	5	0	6	7	0	12	9.14 ± 0.25	0.552
M28	-1.18 ± 0.05	10	10	9	7	7	6	17	5.37 ± 0.10	0.457
NGC 6717	-1.17 ± 0.09	1	1	0	0	0	0	1	7.52 ± 0.13	0.258
M4	-1.12 ± 0.02	31	31	0	14	14	0	45	1.85 ± 0.02	0.385
M5	-1.12 ± 0.01	85	81	75	36	36	35	121	7.48 ± 0.06	0.094
NGC 6401	-1.08 ± 0.06	22	23	15	11	9	7	34	8.06 ± 0.24	1.038
NGC 6284	-1.07 ± 0.05	4	4	0	0	0	0	4	14.21 ± 0.42	0.318
NGC 6642	-1.03 ± 0.17	7	7	0	3	3	0	10	8.05 ± 0.20	0.469
M75	-1.01 ± 0.04	15	13	0	5	6	0	21	20.52 ± 0.45	0.225
M107	-1.00 ± 0.02	15	15	0	6	6	0	21	5.63 ± 0.08	0.424
NGC 6712	-0.97 ± 0.05	7	6	6	6	6	3	13	7.38 ± 0.24	0.414
NGC 6638	-0.89 ± 0.05	3	5	0	9	10	0	15	9.78 ± 0.34	0.424
NGC 6366	-0.59 ± 0.04	1	1	0	0	0	0	1	3.44 ± 0.05	0.730
NGC 6544	-1.37 ± 0.07	1	1	1	0	0	0	1	2.58 ± 0.06	0.767
2MASS-GC02	-1.05 ± 0.16	0	0	0	0	1	1	1	5.50 ± 0.44	1.650
Terzan 10	-0.97 ± 0.16	0	2	2	0	0	0	2	10.21 ± 0.40	2.029
Djorg 2	-0.91 ± 0.05	1	1	0	2	2	0	3	8.76 ± 0.18	1.059
NGC 6540	-0.89 ± 0.73	2	2	2	1	1	1	3	5.91 ± 0.27	0.619
IC 1276	-0.53 ± 0.05	1	1	1	0	0	0	1	4.55 ± 0.25	1.156
NGC 6316	-0.46 ± 0.04	1	1	0	1	1	0	2	11.15 ± 0.39	0.707
NGC 6304	-0.43 ± 0.05	0	0	0	1	1	0	1	6.15 ± 0.15	0.658

**Notes.**

<sup>a</sup> Homogeneous metallicities and distances for each globular cluster were adopted from the GOTHAM survey and Baumgardt & Vasiliev (2021), respectively; see Section 2.2 for more details.

<sup>b</sup> Number of RR Lyrae in a given globular cluster after removing RR Lyrae with  $N < 10$  in all *gri*-band ZTF light curves in our two-iteration template light-curve fitting procedures (see Section 2.4).

<sup>c</sup> Here  $\langle E \rangle$  is the averaged reddening value returned from the Bayerstar2019 3D reddening map (Green et al. 2019) for the RR Lyrae in a given globular cluster, where the number of RR Lyrae used in calculating the averaged reddening value was listed in the  $n_{\text{tot}}$  column.

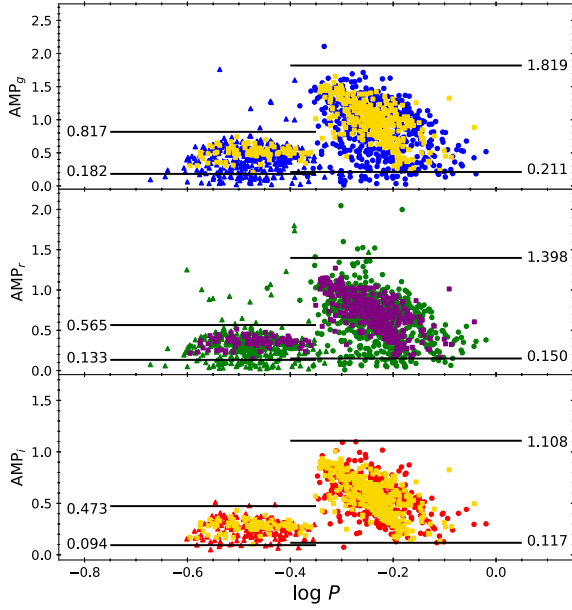


**Figure 3.** Comparison of the amplitudes for the RR Lyrae in our sample (represented in blue, green, and red for the  $gri$  bands, respectively) and the RR Lyrae located in the SDSS Stripe 82 region (adopted from Sesar et al. 2010; gold and purple squares). The RR Lyrae in our sample with type RR0 (or RRab) and RR1 (or RRc) are marked with circles and triangles, respectively. The horizontal lines represent the adopted amplitude cuts in each filter, separated for RR0 and RR1, with values given next to these lines (see text for more details).

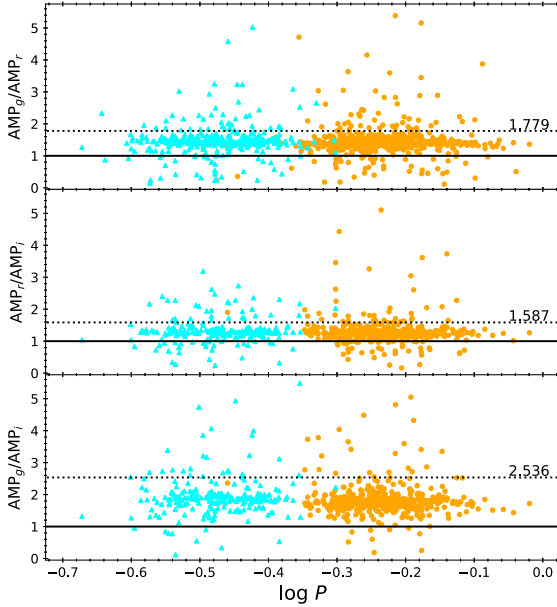


**Figure 4.** The  $gri$ -band amplitude ratios as a function of pulsation period for the RR Lyrae in our sample, marked as filled orange circles and cyan triangles for RR0 and RR1, respectively. The horizontal solid lines represent the amplitude ratios of unity. The dotted lines are the adopted upper limits for the amplitude ratio cuts (see text for more details).

process. We first fit the ZTF light curves with the template light curves, where data points that are more than  $3s$  from the fitted light curves were removed ( $s$  is the dispersion of the fitted light curve<sup>19</sup>), and refit the template light curves on the remaining

<sup>19</sup> We use  $s$  to represent the light-curve dispersion and  $\sigma$  for the dispersion of the PWZ and PLZ relations.

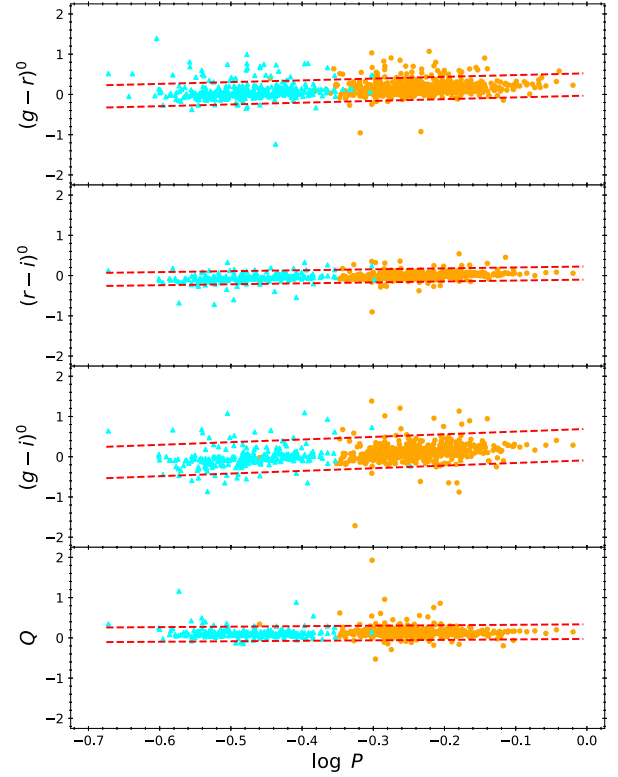


**Figure 5.** Extinction-corrected PC (top three panels) relations and the extinction-free  $Q$ -indices as a function of pulsation period (i.e., the PQ relation; bottom panel) for the RR Lyrae in our sample, separated for RR0 (filled orange circles) and RR1 (filled cyan triangles). The red dashed lines indicate the selection boundaries based on the provisional fitted PC/PQ relations to the RR0 and RR1 combined samples (see text for more details).

data points. The output of our light-curve fitting procedures includes the improved pulsation period  $P$ , the intensity-averaged mean magnitudes  $\langle m \rangle$ , and the amplitudes  $AMP_m$ , where  $m = \{g, r, i\}$  (whenever available), for each RR Lyrae based on the best-fit template light curves.

### 2.5. Error Estimation on Mean Magnitudes

We ran Monte Carlo simulations to evaluate the errors on the mean magnitudes based on our procedures described above. Since template light-curve fitting in *gatspy* is computationally intensive, we selected nine RR Lyrae that have more than 100 data points per light curve, as well as the dispersions on the final fitted light curves that were smaller than 0.05, in all three bands as our sample to run the Monte Carlo simulations. The fitted mean magnitudes of these nine RR Lyrae were considered as the “true values” in our simulations. To create a “simulated” light curve, we randomly selected one RR Lyrae out of the nine, and for this selected RR Lyrae, we randomly picked  $N$  data points without replacement, using a uniform random number generator, from the ZTF light curves. The simulated light curve was fitted with the two-step template light-curve fitting procedure described previously to determine its mean magnitude, which was compared with the true value to determine the difference:  $\Delta_m = FIT_m - TRUE_m$ . We generated 1000 such simulated light curves separately in the  $gri$  bands to build up the distributions of  $\Delta_m$  for  $N$  spanning from 3 to 20. The averaged  $\Delta_m$  and associated standard deviations were then calculated for each  $N$  separately in the  $gri$  bands and presented in Figure 2.

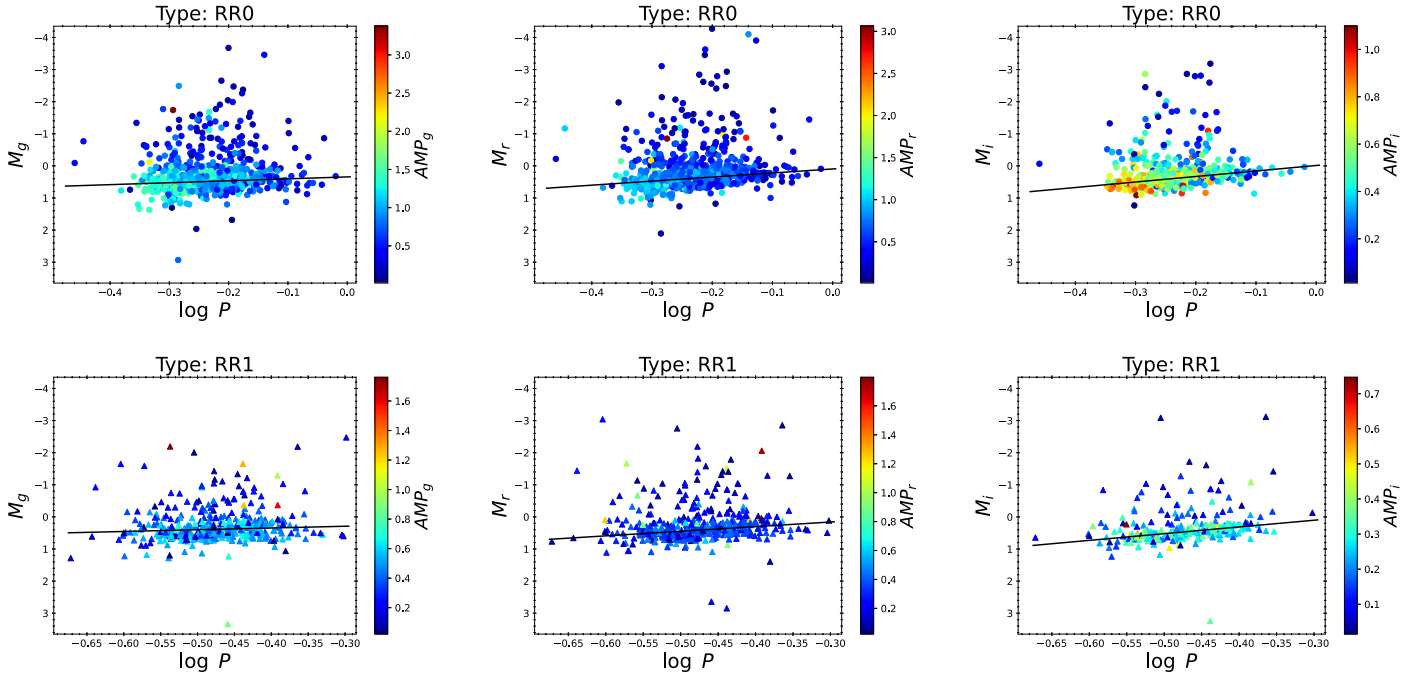


**Figure 6.** Composite *gri*-band PL relations based on the 1209 RR Lyrae in different globular clusters, separated for RR0 (upper panels) and RR1 (lower panels). The solid lines are the provisional fitted PL relations (see text for details). For clarity, error bars are omitted. The colors of the data points represent the amplitudes derived from the best-fit template light curves.

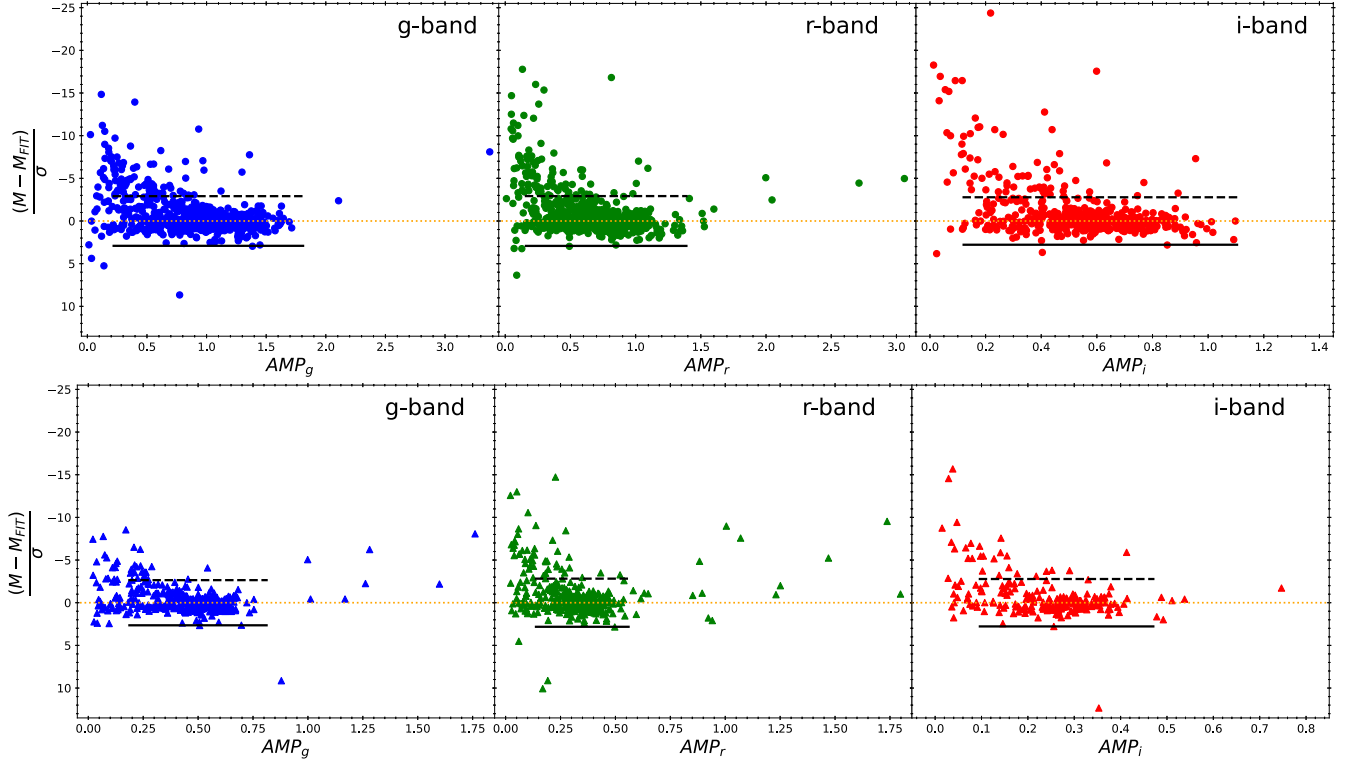


**Figure 7.** Residuals of the fitted PL relations given in Figure 6, in units of the PL dispersion  $\sigma$ , as a function of the light-curve amplitudes. The orange dotted horizontal line represents the zero residuals to guide the eye. The solid horizontal lines are the boundaries on the positive residuals determined using the `boundfit` code (Cardiel 2009; see text for more details). The dashed horizontal lines are the boundaries on the negative residuals mirrored from the solid horizontal lines. The sizes of these horizontal lines were based on the adopted amplitude cuts (see Figure 3). Upper and lower panels are for RR0 (filled circles) and RR1 (filled triangles), respectively.

It is clear from Figure 2 that the largest averaged  $\Delta_m$  and standard deviation occurred when  $N = 3$ ; hence, the template light-curve fitting should not be applied to light curves with only three data points. In the case of a small number of

clustered data points, the template fits can give very large amplitudes, resulting in unrealistically large scatter in the mean magnitudes. Furthermore, the averaged  $\Delta_m$  values exhibit a trend for  $N < 10$  and stabilized when  $N \geq 10$  with values

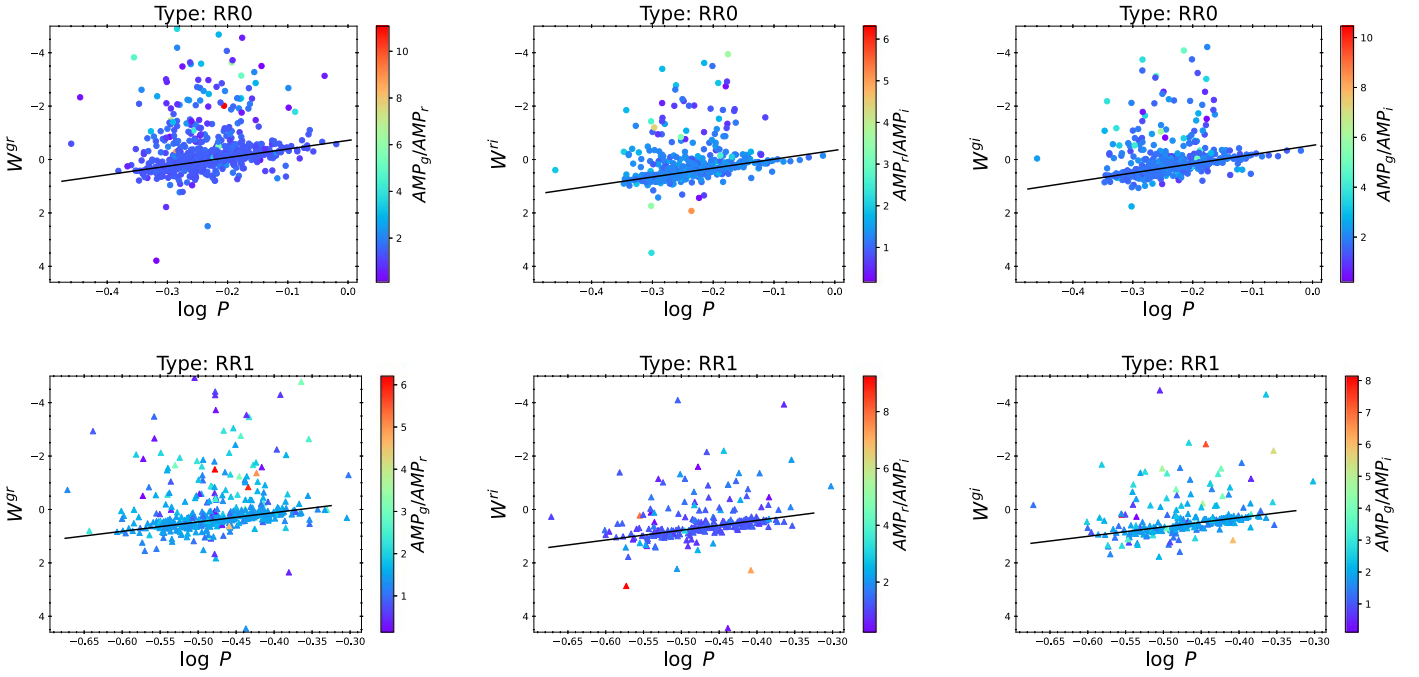


**Figure 8.** Composite PW relations based on the 1209 RR Lyrae in different globular clusters, separated for RR0 (upper panels) and RR1 (lower panels). The solid lines are the provisional fitted PW relations (see text for details). For clarity, error bars are omitted. The colors of the data points represent the amplitude ratios derived from the best-fit template light curves.

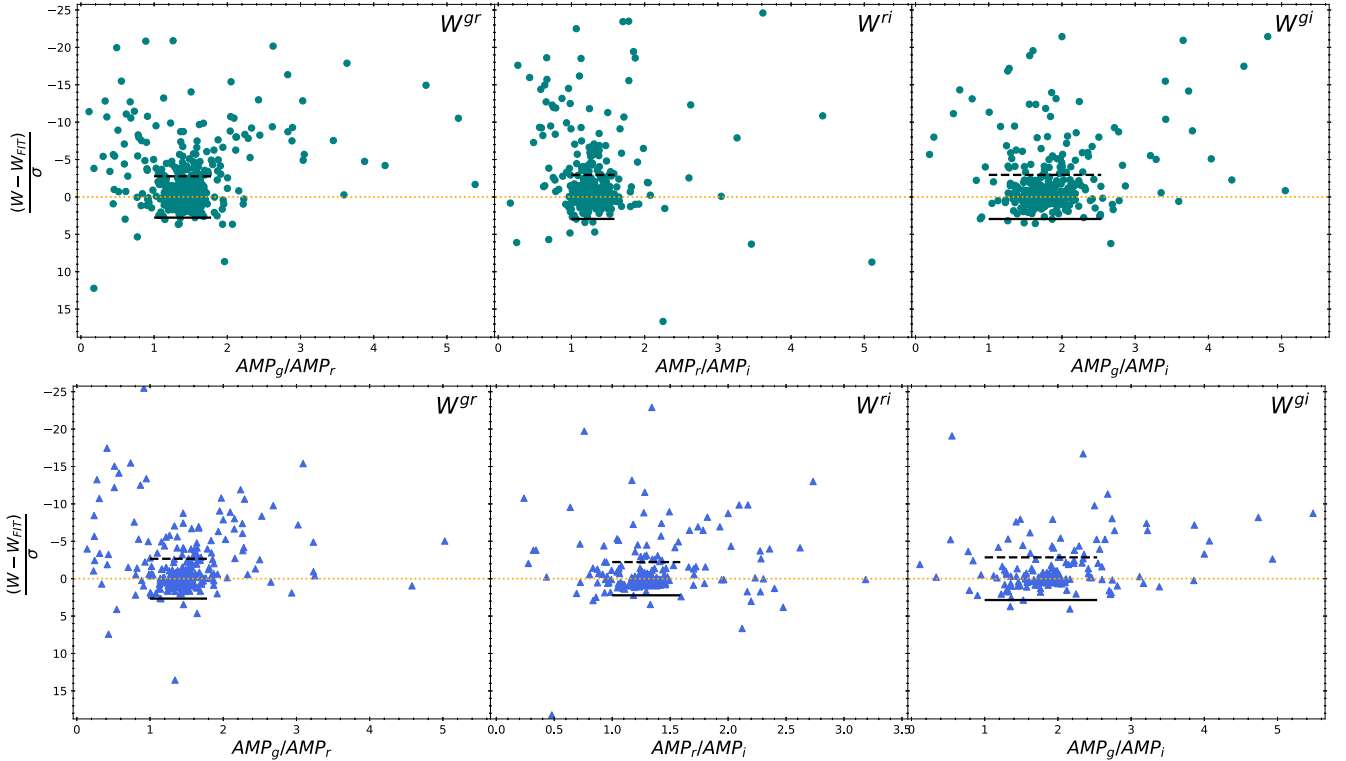


**Figure 9.** Residuals of the fitted PW relations given in Figure 8, in units of the PW dispersion  $\sigma$ , as a function of the amplitude ratios. The orange dotted horizontal line represents the zero residuals to guide the eye. The solid horizontal lines are the boundaries on the positive residuals determined using the `boundfit` code (Cardiel 2009; see text for more details). The dashed horizontal lines are the boundaries on the negative residuals mirrored from the solid horizontal lines. The sizes of these horizontal lines were based on the adopted amplitude ratio cuts (see Figure 4). The upper and lower panels are for RR0 (filled circles) and RR1 (filled triangles), respectively.

within  $\pm 0.005$  mag. Hence, the template light-curve fitting procedures should only be applied to light curves with  $N \geq 10$ . Large standard deviations can be seen when  $N$  is less than 9 and decrease substantially for large  $N$ . An exponential decay

function in the form of  $f(N) = 0.187e^{-0.131N}$  can be used to fit the standard deviations when  $N \geq 10$ . Therefore, the calculated values of the standard deviation based on  $f(N)$  are 0.051 mag at  $N = 10$ , reduced to 0.014 mag at  $N = 20$ , and smaller than

**Table 3**  
Periods, Mean Magnitudes, Amplitudes, and Reddenings for Our Sample of RR Lyrae

Var. Name <sup>a</sup>	Type <sup>b</sup>	Period (days)	$\langle m_g \rangle$	AMP <sub>g</sub>	N <sub>g</sub>	$\langle m_r \rangle$	AMP <sub>r</sub>	N <sub>r</sub>	$\langle m_i \rangle$	AMP <sub>i</sub>	N <sub>i</sub>	E	Flag
Palomar3_V2	RR0	0.59867205	20.512	0.742	92	20.301	0.597	121	20.215	0.293	10	0.004 ± 0.002	A_
Palomar3_V3	RR0	0.56690511	20.469	0.872	107	20.269	0.661	120	20.150	0.431	12	0.004 ± 0.002	_R
Palomar3_V5	RR0	0.58168014	20.518	0.846	97	20.327	0.585	128	20.209	0.379	10	0.004 ± 0.002	—
Palomar3_V6	RR0	0.59336755	20.493	0.916	83	20.311	0.583	60	−99.999	−9.999	7	0.004 ± 0.002	—
...	...	...	...	...	...	...	...	...	...	...	...	...	...

**Notes.** Table 3 is published in its entirety in machine-readable format. A portion is shown here for guidance regarding its form and content. The AMP<sub>{g,r,i}</sub> is the amplitude based on the best-fit template light curve. Values of −99.990 and −9.990 denote no data or rejected light curves. The N<sub>{g,r,i}</sub> is the number of data points in a given filter after the two-step template fitting processes as described in Section 2.3. The E is the reddening value returned from the Bayerstar2019 3D reddening map (Green et al. 2019) using the globular cluster distance listed in Table 2.

<sup>a</sup> The format for the names of the RR Lyrae in globular clusters is [GC]\_[RRL Name], where [RRL Name] is adopted from Clement’s Catalog. Note that we renamed 23 P1 in NGC 6712 as 23\_ P1 in our table.

<sup>b</sup> Pulsation types for RR Lyrae, either RR0 (for fundamental mode) or RR1 (for first-overtone mode).

(This table is available in its entirety in machine-readable form.)

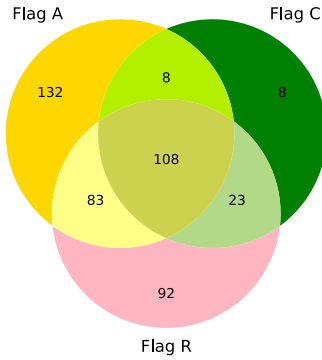


**Figure 10.** Venn diagram for the excluded RR Lyrae in our sample (see text for details on flags A, C, and R).

0.001 mag when  $N > 40$ . Standard deviations calculated from  $f(N)$  would be adopted as an error estimate for the mean magnitudes.

### 3. Further Filtering of RR Lyrae Sample

Based on the results obtained in Section 2.5, we removed 120 RR Lyrae that have  $N < 10$  in all three filters after the second iteration in our template light-curve fitting procedure, which leaves 1209 RR Lyrae in our sample. These remaining RR Lyrae are located in 54 globular clusters, as summarized in Table 2, along with their number and the metallicity, extinction, and distance to each cluster. We further visually inspected a subset of the light curves for this sample of RR Lyrae and found that a fraction of the fitted light curves were problematic. For example, some of these problematic light curves contain a small number of data points that cluster at certain pulsational phases or have mismatched data points from very close by neighboring sources (due to the crowded nature of globular clusters). In many cases, these problematic light curves were found to be caused by blending. Due to the highly crowded nature of globular clusters, blending is an unavoidable issue for RR Lyrae located near the center, or core, of the globular clusters. The inclusion of the fluxes from very close and yet unresolved constant stars will have two effects on the RR Lyrae light curves: the RR Lyrae will appear brighter, and the amplitudes of the RR Lyrae light curves will be greatly “damped” or reduced. A similar discussion of Cepheid’s light curve due to blending can be found in Riess et al. (2020). Therefore, those RR Lyrae affected by blending, as well as other problematic light curves, should be excluded.

#### 3.1. Filtering Based on Amplitudes

We first examined the amplitudes of the RR Lyrae that remained in our sample. Since the light-curve amplitudes for pulsating stars cannot be arbitrarily large, fitted light curves with large amplitudes indicated that there were some problems related to the sampling of the light curves. Similarly, if the light-curve amplitudes were too small, this would hint at the presence of blending. The *gri*-band amplitudes for our sample of RR Lyrae are shown in Figure 3, overlaid with a sample of 483 RR Lyrae located in the Sloan Digital Sky Survey (SDSS) Stripe 82 region (Sesar et al. 2010). The SDSS Stripe 82 RR Lyrae samples are located in the Galactic halo; hence, they are expected to be unaffected by blending. Clearly, amplitudes for some of our sample of RR Lyrae were either larger or smaller than those laid out by the SDSS Stripe 82 RR Lyrae, which can be used to define the amplitude cuts. To account for the possibility that the RR Lyrae in the globular clusters may have larger amplitudes, the maximum amplitudes found in the SDSS Stripe 82 RR Lyrae were then increased by 10% and adopted as the maximum amplitude cuts. Similarly, the minimum amplitude cuts were based on the minimum amplitudes found in the SDSS Stripe 82 RR Lyrae but decreased by 10%. These adopted amplitude cuts are shown as horizontal lines in Figure 3.

Amplitude ratios between different filters can also be used to filter out the problematic light curves. Figure 4 presents the derived amplitude ratios for our sample of RR Lyrae, at which the majority of the RR Lyrae fall in a tight sequence. Since the amplitudes for RR Lyrae are larger at shorter-wavelength filters (for example, see Braga et al. 2016; Bhardwaj et al. 2020), amplitude ratios as defined in Figure 4 should have values larger than unity (indicated with solid lines in Figure 4). However, there are a number of outliers with unusually large amplitude ratios. Therefore, we first exclude those RR Lyrae in our sample with amplitude ratios smaller than unity; the remaining RR Lyrae were used to estimate the averaged amplitude ratios via an iterative  $3\sigma$  clipping algorithm, which were found to be:

$$\left\langle \frac{\text{AMP}_g}{\text{AMP}_r} \right\rangle = 1.419, \quad \left\langle \frac{\text{AMP}_g}{\text{AMP}_i} \right\rangle = 1.266, \quad \left\langle \frac{\text{AMP}_r}{\text{AMP}_i} \right\rangle = 1.782,$$

with corresponding standard deviations of 0.120, 0.107, and 0.251, respectively. The lower limit of the amplitude ratio cut is 1. For the upper limit, we adopted a value that is three times the standard deviation larger than the averaged amplitude ratio,

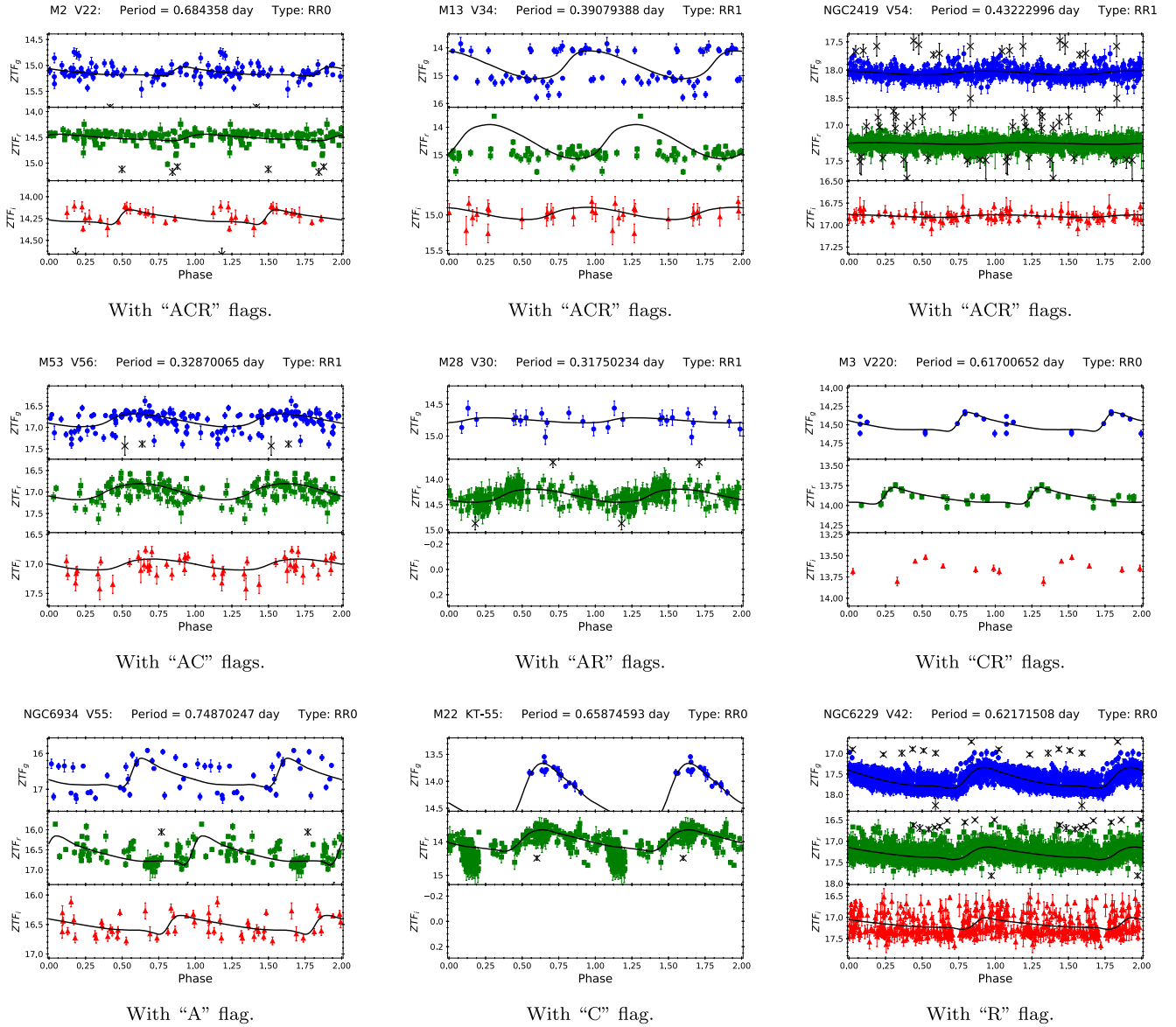


**Figure 11.** Examples of the light curves for RR Lyrae with three (top panels), two (middle panels), and one (bottom panels) ACR flag. The black crosses are rejected data points during the first pass of the two-iteration template light-curve fitting procedure, and the black curves are the best-fit template light curves after the second pass of the procedure (see Section 2.4 for more details).

indicated by the dotted lines in Figure 4. While deriving these averaged values (and their standard deviations), we did not separate out RR0 and RR1 because the derived averaged values do not show a significant deviation between them (for example, the averaged  $gr$ -band amplitude ratios are 1.405 and 1.452 for RR0 and RR1, respectively).

Combining the amplitude cuts given in Figure 3 and the amplitude ratio cuts shown in Figure 4 (dotted and solid lines), there are 331 RR Lyrae in our sample (out of 1209) that did not satisfy the selection criteria based on either the amplitudes, amplitude ratios, or both. These RR Lyrae were flagged as “A” in our sample.

### 3.2. Filtering Based on Colors

As pulsating stars, RR Lyrae are expected to obey a period–color (PC) relation. Therefore, outliers presented on the plot of the PC relation indicate that their corresponding light curves

could be problematic. The top panels of Figure 5 present the extinction-corrected PC relations for the RR Lyrae in our sample, at which the mean magnitudes in each filter were corrected using  $R_{\{g,r,i\}}E$ . The values of the extinction coefficient are  $R_{\{g,r,i\}} = \{3.518, 2.617, 1.971\}$  (Green et al. 2019) because ZTF photometry is calibrated to the Pan-STARRS1 system (Masci et al. 2019), and the reddening  $E$  toward each of the RR Lyrae was obtained using the Bayerstar2019 3D reddening map (Green et al. 2019; see Section 2.2).

In Figure 5, the majority of the RR Lyrae show a tight and continuous PC relation for the RR0 and RR1 combined sample, but outliers were also presented in these PC relations. Most of these outliers had either amplitude or amplitude ratios beyond the respected cuts as defined in the previous subsection. To remove these outliers, an iterative linear regression with a  $3\sigma$  outlier rejection algorithm was applied to fit both RR0 and RR1. The  $3\sigma$  boundaries from the provisional fitted PC relations, displayed as dashed lines in Figure 5, were adopted

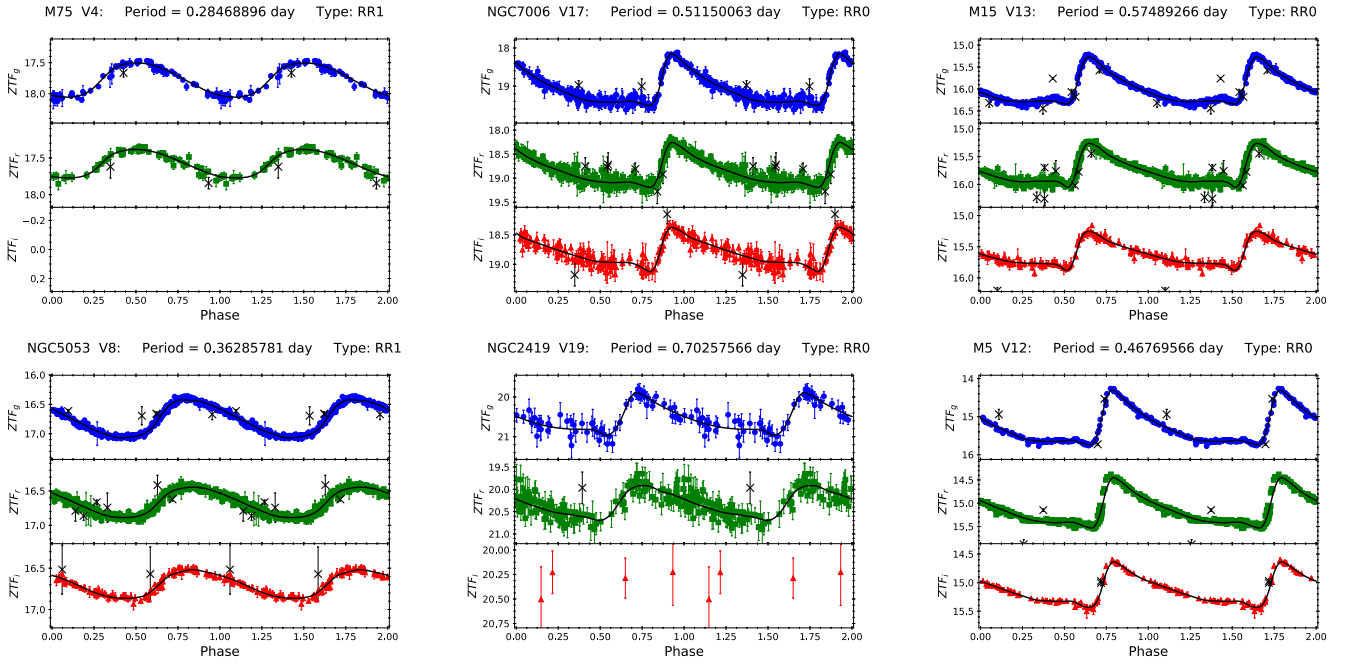


**Figure 12.** Examples of the randomly selected light curves for RR Lyrae without any flags. The black crosses are rejected data points during the first pass of the two-iteration template light-curve fitting procedure, and the black curves are the best-fit template light curves after the second pass of the procedure (see Section 2.4 for more details).

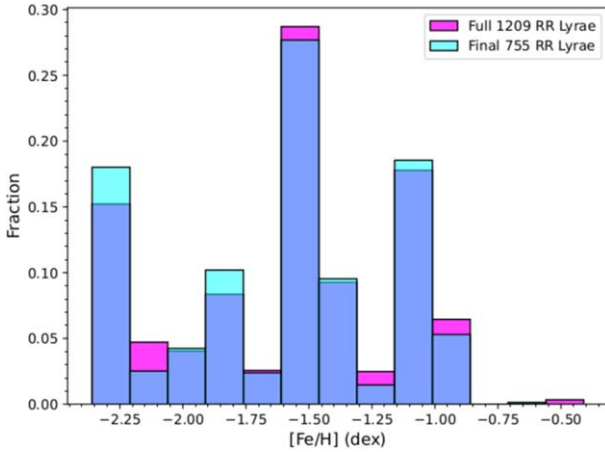


**Figure 13.** Histograms of [Fe/H] distribution for the full sample of 1209 RR Lyrae and the remaining sample of 755 RR Lyrae. The [Fe/H] values for the RR Lyrae are based on their host globular clusters (see Table 2).

as the period-dependent color cuts. Note that fitting of the PC relations separately for RR0 and RR1 in our final sample will be done in Section 5.

To circumvent the possibility that the outliers shown in Figure 5 were (partly) due to the extinction, we plotted the extinction-free  $Q$ -indices as a function of pulsation period in the bottom panel of Figure 5 for RR Lyrae that have mean magnitudes in all  $gri$  bands. Given the adopted values of  $R_{\{g,r,i\}}$ , the extinction-free  $Q$ -index is defined as

$$Q = (g - r) - 1.395(r - i).$$

Similar to the PC relations, we derived a provisional period- $Q$ -index (PQ) relation, and the  $3\sigma$  boundaries were adopted as the period-dependent  $Q$ -index cuts, shown as the dashed lines in the bottom panel of Figure 5.

In total, there are 147 RR Lyrae located outside the  $3\sigma$  boundaries of either the three PC relations or the PQ relation. These RR Lyrae were flagged as “C” in our sample.

### 3.3. Filtering Based on PL/PW Residuals

Figure 6 presents the extinction-corrected  $gri$ -band PL relations for our sample of RR Lyrae. The mean magnitudes  $\langle m \rangle$  for these RR Lyrae were converted to absolute magnitudes using  $M_{\{g,r,i\}} = \langle m_{\{g,r,i\}} \rangle - R_{\{g,r,i\}}E - 5 \log D + 5$ , where the extinction term ( $R_{\{g,r,i\}}E$ ) was described in Section 3.2, and the distance  $D$  was adopted from Baumgardt & Vasiliev (2021; see Section 2.2). Errors from  $\langle m \rangle$ ,  $E$ , and  $D$  were propagated to the total errors on  $M$ .

As mentioned, blending would cause an RR Lyrae to appear brighter; at the same time, the amplitude of such an RR Lyrae would be reduced. As can be seen from Figure 6, there are a number of RR Lyrae that seem to be brighter than the rest of the RR Lyrae at a given period. These RR Lyrae also tend to have smaller amplitudes obtained from the best-fit template light curves, suggesting that they were most likely affected by blending and should be excluded. A provisional PL relation in the form of  $M_{\text{FIT}} = a \log P + b$ , separately for RR0 and RR1, was fitted to our sample of RR Lyrae, where the fitting was performed using an iterative  $3\sigma$  rejection procedure to remove the outliers until the fitted parameters  $a$  and  $b$  converged. The fitted provisional PL relations are shown as solid lines in Figure 6.

To better visualize the effects of blending, the residuals of the fitted PL relations, in units of PL dispersion  $\sigma$ , i.e.,  $(M - M_{\text{FIT}})/\sigma$ , were plotted against the amplitudes determined from the best-fit template light curves in Figure 7, showing that more negative residuals (i.e., brighter than expected) tend to have a smaller amplitude. After excluding RR Lyrae with  $(M - M_{\text{FIT}})/\sigma > 3$  (based on the adopted iterative  $3\sigma$  rejection linear regression fitting) and those with amplitudes outside the

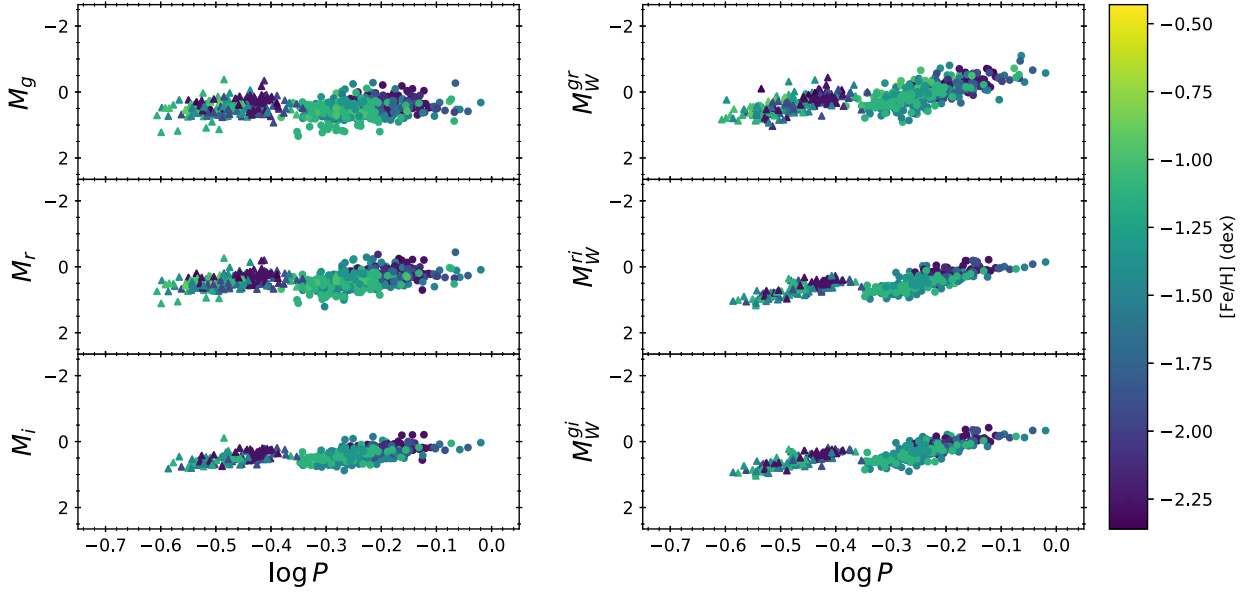


**Figure 14.** The PL relations (left panels, after correction for extinction) and PW relations for all of the RR Lyrae listed in Table 3 by adopting the distance of the globular clusters as listed in Table 2. The color bar represents the metallicity of the host globular clusters. Circles and triangles are for the RR Lyrae with pulsation types of RR0 and RR1, respectively. Error bars are omitted for clarity.

amplitude cuts defined in Figure 3, we determined the one-site boundaries on the positive residuals by using the `boundfit` code<sup>20</sup> (Cardiel 2009). These boundaries are indicated by solid horizontal lines in Figure 7. Since the residuals of the PL relation should be symmetric, these boundaries were then mirrored from the negative residuals and presented as dashed horizontal lines in Figure 7. The RR Lyrae with negative residuals that were more negative than the dashed horizontal lines are brighter than expected, implying that they could be affected by blending (which also tends to have smaller amplitudes).

In addition to the PL relations, we have also examined the PW relation for our sample of RR Lyrae. The extinction-free Wesenheit indices were defined as (Ngeow et al. 2021)

$$\begin{aligned} W^{gr} &= r - 2.905(g - r), \\ W^{ri} &= r - 4.051(r - i), \\ W^{gi} &= g - 2.274(g - i). \end{aligned}$$

The corresponding PW relations are presented in Figure 8, together with the provisional PW relations (fitted with the same iterative  $3\sigma$  rejection algorithm as in the case of provisional PL relations), shown by solid lines. The data points in Figure 8 were also color-coded with amplitude ratios. There are two features revealed in Figure 8. First of all, the majority of the outliers are brighter than those RR Lyrae located along the ridgelines at a given period, again indicating the presence of blending. Second, the RR Lyrae along the ridgelines have similar or consistent amplitude ratios, while the outliers have either a large or a small (i.e., smaller than unity) amplitude ratio.

The residuals of the provisional PW relations, in units of PW dispersion  $\sigma$ , as a function of amplitude ratio are presented in Figure 9. It is clear that RR Lyrae with small PW residuals (e.g.,  $<|3\sigma|$ ) also tend to concentrate on a small range of amplitude ratios, iterating the similar concentration in Figure 4. Similar to the PL residuals, we used `boundfit` to determine

the one-site boundaries on the positive residuals after excluding the outlying residuals with  $(W - W_{\text{FIT}})/\sigma > 3$  and outside the amplitude ratio cuts given in Figure 4. The determined one-site boundaries were then mirrored from the negative residuals. These boundaries are shown as solid and dashed horizontal lines in Figure 9.

Based on the residuals from the PL or PW relations, there were 306 RR Lyrae with residuals beyond the boundaries determined in either Figure 7 or Figure 9 (both solid and dashed lines). These RR Lyrae were flagged as “R” in our sample.

### 3.4. The Final Sample of RR Lyrae

The refined periods and reddenings, as well as the mean magnitudes, amplitudes, and number of data points left in the *gri*-band light curves for the 1209 RR Lyrae in our sample, are presented in Table 3. In the last column of Table 3, we also include the flags for each RR Lyrae based on the analysis given in the previous subsections. Out of the 1209 RR Lyrae in our sample, 108 have all three ACR flags. The number of RR Lyrae with two flags is 114 (8, 23, and 83 with AC, CR, and AR, respectively), while the number of RR Lyrae with only one flag is 232 (132, 8, and 92 with A, C, and R, respectively). A Venn diagram showing the distribution of these flagged RR Lyrae is presented in Figure 10. Example light curves for these flagged RR Lyrae are shown in Figure 11 for the cases with three, two, and one flag, showing that the light curves for RR Lyrae with any of the ACR flags or a combination of them were problematic for a variety of reasons and should be excluded.

The remaining 755 RR Lyrae in our sample do not carry any of the ACR flags. Examples of their light curves are presented in Figure 12, demonstrating the good quality of the ZTF light curves for them. These samples of RR Lyrae will be used to derive the PLZ and PWZ relations in the next section, and they are located in 46 (out of 54) globular clusters. The excluded globular clusters are (as listed in the bottom of Table 2) 2MASS-GC02, Djorg 2, IC 1276, NGC 6304, NGC 6316, NGC 6540, NGC 6544, and Terzan 10, as all of their RR Lyrae

<sup>20</sup> <https://github.com/nicocardiel/boundfit>

**Table 4**  
Fitted Coefficients for Various Relations

	$a$	$b$	$c$	$\sigma$	$N_{\text{ini}}/N_{\text{fit}}$
RR0 Only					
$M_g$	$0.649 \pm 0.073$	$-0.302 \pm 0.193$	$0.159 \pm 0.024$	0.227	493/490
$M_r$	$0.337 \pm 0.059$	$-1.090 \pm 0.154$	$0.139 \pm 0.020$	0.187	516/508
$M_i$	$0.243 \pm 0.055$	$-1.432 \pm 0.144$	$0.144 \pm 0.018$	0.148	326/321
$W^{gr}$	$-0.644 \pm 0.058$	$-3.324 \pm 0.155$	$0.052 \pm 0.020$	0.205	483/478
$W^{ri}$	$0.093 \pm 0.051$	$-2.600 \pm 0.133$	$0.193 \pm 0.017$	0.145	326/325
$W^{gi}$	$-0.198 \pm 0.054$	$-2.908 \pm 0.142$	$0.142 \pm 0.018$	0.146	325/323
$(g - r)$	$0.333 \pm 0.023$	$0.764 \pm 0.060$	$0.035 \pm 0.007$	0.076	483/483
$(r - i)$	$0.040 \pm 0.014$	$0.361 \pm 0.038$	$-0.017 \pm 0.004$	0.035	326/323
$(g - i)$	$0.323 \pm 0.033$	$1.110 \pm 0.088$	$-0.001 \pm 0.010$	0.093	325/325
$Q$	$0.222 \pm 0.016$	$0.220 \pm 0.044$	$0.042 \pm 0.005$	0.046	325/320
RR1 Only					
$M_g$	$0.411 \pm 0.166$	$-0.342 \pm 0.289$	$0.092 \pm 0.028$	0.189	218/212
$M_r$	$-0.082 \pm 0.138$	$-1.393 \pm 0.238$	$0.091 \pm 0.024$	0.164	227/224
$M_i$	$-0.205 \pm 0.139$	$-1.706 \pm 0.246$	$0.077 \pm 0.023$	0.128	123/122
$W^{gr}$	$-1.327 \pm 0.143$	$-3.680 \pm 0.248$	$0.013 \pm 0.024$	0.172	216/210
$W^{ri}$	$-0.884 \pm 0.141$	$-3.503 \pm 0.249$	$0.067 \pm 0.023$	0.132	123/123
$W^{gi}$	$-1.086 \pm 0.126$	$-3.696 \pm 0.223$	$0.055 \pm 0.020$	0.111	123/120
$(g - r)$	$0.398 \pm 0.059$	$0.781 \pm 0.103$	$0.017 \pm 0.009$	0.069	216/215
$(r - i)$	$0.194 \pm 0.039$	$0.569 \pm 0.070$	$-0.005 \pm 0.006$	0.030	123/121
$(g - i)$	$0.670 \pm 0.101$	$1.545 \pm 0.179$	$0.014 \pm 0.016$	0.080	123/122
$Q$	$0.192 \pm 0.029$	$0.162 \pm 0.052$	$0.024 \pm 0.004$	0.039	123/121
RR0 + RR1					
$M_g$	$0.801 \pm 0.048$	$-0.032 \pm 0.110$	$0.190 \pm 0.019$	0.216	711/704
$M_r$	$0.432 \pm 0.039$	$-0.874 \pm 0.089$	$0.154 \pm 0.016$	0.180	743/731
$M_i$	$0.249 \pm 0.041$	$-1.362 \pm 0.093$	$0.115 \pm 0.016$	0.138	449/444
$W^{gr}$	$-0.727 \pm 0.041$	$-3.286 \pm 0.093$	$0.010 \pm 0.016$	0.191	699/687
$W^{ri}$	$0.010 \pm 0.037$	$-2.756 \pm 0.086$	$0.149 \pm 0.015$	0.130	448/444
$W^{gi}$	$-0.288 \pm 0.039$	$-3.066 \pm 0.090$	$0.101 \pm 0.015$	0.137	449/444
$(g - r)$	$0.333 \pm 0.014$	$0.803 \pm 0.034$	$0.030 \pm 0.005$	0.073	699/697
$(r - i)$	$0.063 \pm 0.009$	$0.428 \pm 0.023$	$-0.012 \pm 0.003$	0.033	449/444
$(g - i)$	$0.370 \pm 0.022$	$1.263 \pm 0.055$	$0.007 \pm 0.007$	0.089	448/447
$Q$	$0.218 \pm 0.009$	$0.222 \pm 0.023$	$0.038 \pm 0.003$	0.043	448/440

**Note.** The fitting parameters  $a$ ,  $b$ , and  $c$  are defined in Equation (1), and  $\sigma$  is the dispersion of the fitted relation. Here  $N_{\text{ini}}$  and  $N_{\text{fit}}$  are the number of RR Lyrae before and after applying the  $3\sigma$  rejection algorithm (the number of rejected RR Lyrae varies from zero to 12). Note that  $M_{gri}$  and various colors have been corrected for extinction.

have one or more flags. These also removed the three globular clusters with the highest metallicities (IC 1276, NGC 6316, and NGC 6304); hence, the range of metallicity covered by the 755 RR Lyrae is from  $-2.36$  to  $-0.54$  dex, with a median of  $-1.48$  dex. Figure 13 compares the metallicity distribution between the full sample of 1209 RR Lyrae and the remaining sample of 755 RR Lyrae; no substantial difference can be seen between their distributions. This ensures there is no bias introduced when fitting the PLZ and PWZ relations to the remaining 755 RR Lyrae sample.

#### 4. The PLZ and PWZ Relations

The extinction-corrected  $gri$ -band PL and PW relations for the final sample of 755 RR Lyrae are presented in the left and right panels of Figure 14, respectively, where the colors represent the metallicity of the host globular clusters. These RR Lyrae were fitted with PLZ and PWZ relations in the following form:

$$y = a + b \log P + c[\text{Fe}/\text{H}], \quad (1)$$

where  $y$  is either  $M_{gri}$  or  $W$ , and all RR Lyrae in a given cluster are assumed to have the same distance as in Table 2. We solved

Equation (1) using a  $\chi^2$  minimization within a matrix formalism of dependent and independent parameters, including their associated uncertainties in the covariance matrix (similar to Equation (5) in Bhardwaj et al. 2016). As in Bhardwaj et al. (2021), we also applied an iterative  $3\sigma$  rejection algorithm to remove the single largest outlier in each iteration until convergence. Figure 14 shows that there are still a few outliers presented in the PL and PW relations that were not flagged based on the selection criteria presented in Section 3. Their light curves look normal, implying that other physical reasons (such as locating in front of or behind the host globular clusters, incorrect estimation of extinction, etc.) are causing them to become outliers on the PL and/or PW relations. Nevertheless, they should be excluded to obtain a more robust relation. The fitted coefficients and the corresponding dispersion are summarized in Table 4 for RR0 and RR1 separately, as well as the RR0 and RR1 combined sample. When combining the RR0 and RR1 samples, the periods for RR1 were fundamentalized using  $\log P_0 = \log P_1 + 0.127$  (for example, see Iben 1974; Coppola et al. 2015), where  $P_1$  and  $P_0$  represent

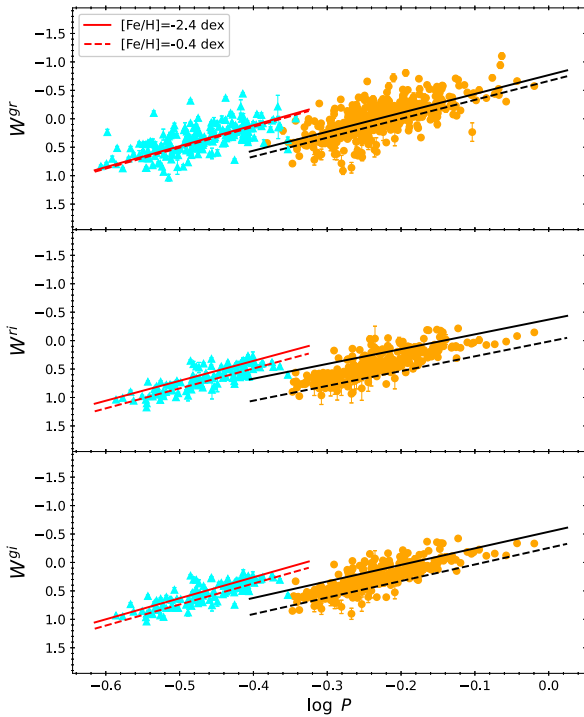


**Figure 15.** Metallicity-dependent PWZ relations for our sample of RR Lyrae. The solid and dashed lines (both red and black) represent the PWZ relations evaluated at  $[\text{Fe}/\text{H}] = -2.4$  and  $-0.4$  dex, respectively. The orange circles and cyan triangles are for RR0 and RR1, respectively. The PWZ relations for the combined sample of RR0 and RR1 (after fundamentalizing the periods) are similar; hence, they are not included in this figure.

the first-overtone period and the corresponding fundamentalized period.

In Figure 15, we present the fitted PWZ relations evaluated at  $[\text{Fe}/\text{H}] = -2.4$  and  $-0.4$  dex. These two values of metallicity were chosen to bracket the metallicity listed in Table 2. As can be seen from Figure 15 and Table 4, the  $W^{gr}$  PWZ relations show a very weak, or even vanishing, dependence on the metallicity for either RR0 or RR1 or the combined sample. Interestingly, similar metallicity-independent PW(Z) relations were found in Marconi et al. (2015) for Wesenheit indices defined in the Johnson  $BVR$  filters based on a series of theoretical models. We noted that the  $gr$ -band transmission curves cover a similar wavelength range as the Johnson  $BVR$ -band transmission curves. As discussed in Marconi et al. (2015), such a nearly metallicity-independent PW(Z) relation can be used as a robust distance indicator; however, the downside is that our derived  $W^{gr}$  PWZ relations exhibit a larger dispersion than other two Wesenheit indices. Based on Table 4, we also notice that the fitted PLZ and PWZ relations involving the  $i$  band have the smallest dispersion.

In the following subsections, we compared our derived PLZ relations to published PL(Z) relations in the  $gri$  bands, including three empirical and two theoretical PL(Z) relations. For ease of comparison, we summarize the slopes of these PL(Z) relations in Table 5.

#### 4.1. Comparisons to Published Results: Empirical Relations

Sesar et al. (2017) derived PLZ relations in the  $gri(z)$  bands using a sample of 55 RR0 located in five globular clusters. We compare the  $gri$ -band PLZ relations derived in their work with ours in Figure 16 and find that these two sets of PLZ relations disagree with each other. For example, the metallicity terms for

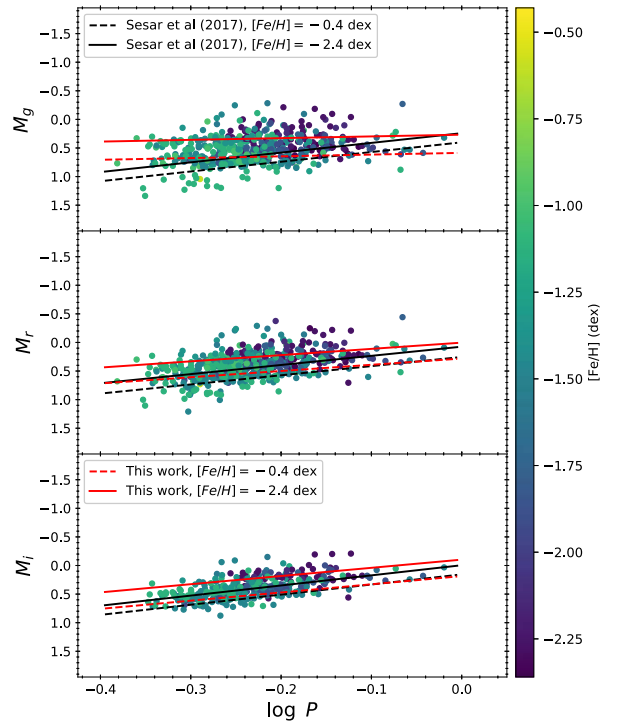


**Figure 16.** Comparison of the PLZ relations for RR0 from Sesar et al. (2017; black) and this work (i.e., Table 4; red) evaluated at two metallicities,  $[\text{Fe}/\text{H}] = -2.4$  and  $-0.4$  dex, as solid and dashed lines, respectively.

our PLZ relations are approximately twice the values reported in Sesar et al. (2017). The slopes of these PLZ relations even show a larger disagreement, especially for the  $g$ -band PLZ relations. Our  $i$ -band PLZ relation has a slope closer to the one derived in Sesar et al. (2017;  $-1.432$  versus  $-1.77$ ); however, these two slopes are different by  $\sim 2\sigma$ . The photometric system used in Sesar et al. (2017) is in the Pan-STARRS1 system, which is the same as the ZTF, also in the Pan-STARRS1 system, and our work is significantly different, including the data sources used, the adopted distances to the globular clusters, and the methodology of fitting the PLZ relations. Using a Bayesian inference approach, Sesar et al. (2017) adopted a tight Gaussian prior when fitting the slopes of the  $ri$ -band PLZ relations but not the  $g$  band. This might explain why the slope of the  $g$ -band PLZ relation is much steeper in Sesar et al. (2017) than our derived value as presented in Table 4.

A similar comparison was also done on the PL relations derived in Vivas et al. (2017) using RR Lyrae in M5 observed with DECam. As is evident in Figure 17, these two sets of PL relations are in remarkably good agreement for both RR0 and RR1 PL relations. Vivas et al. (2017) calibrated their photometry to the native DECam system, which has been extensively employed by the Dark Energy Survey (DES; Dark Energy Survey Collaboration et al. 2016); therefore, the PL relations presented in Vivas et al. (2017) are, strictly speaking, in the DES photometric system. To transform the PL relations given in Vivas et al. (2017) from the DES system to the Pan-STARRS1 system, we added a correction term  $\delta_m$  to their PL relations separately in the  $gri$  bands for RR0 and RR1. These  $\delta_m$  were determined using the averaged colors of RR0 and RR1 based on the  $\sim 60$  RR Lyrae listed in Vivas et al. (2017), together with the transformation provided in Abbott et al. (2021), and found to be small (ranging from  $-0.024$  to  $+0.005$  mag). We have also checked the mean magnitudes between our work and Vivas et al. (2017) by transforming the mean

**Table 5**  
Comparison of the Slopes of PL(Z) Relations from Various Studies

Ref.	<i>g</i> -band	<i>r</i> -band	<i>i</i> -band	Globular Cluster (GC)
For RR0				
TW	$-0.302 \pm 0.193$	$-1.090 \pm 0.154$	$-1.432 \pm 0.144$	46 GCs
S17	$-1.7 \pm 0.3$	$-1.6 \pm 0.1$	$-1.77 \pm 0.08$	5 GCs
V17	$-0.57 \pm 0.17$	$-1.28 \pm 0.11$	$-1.59 \pm 0.09$	M5
B21	$-0.111 \pm 0.160$	...	$-1.292 \pm 0.184$	M15
C08	...	...	1.035	...
M06 <sup>a</sup>	-0.311	...	...	...
For RR1				
TW	$-0.342 \pm 0.289$	$-1.393 \pm 0.238$	$-1.706 \pm 0.246$	46 GCs
V17	$-0.72 \pm 0.32$	$-1.35 \pm 0.21$	$-1.61 \pm 0.16$	M5
B21	$-0.019 \pm 0.138$	...	$-1.329 \pm 0.112$	M15
M06 <sup>a</sup>	-0.322	...	...	...
For RR0+RR1				
TW	$-0.032 \pm 0.110$	$-0.874 \pm 0.089$	$-1.362 \pm 0.093$	46 GCs
B21	$+0.185 \pm 0.066$	...	$-1.222 \pm 0.060$	M15

**Notes.** Slopes without errors are for the (semi)theoretical PL(Z) relations. In case of RR0+RR1, periods for RR1 have been fundamentalized. The references are as follows: TW = this work (Table 4); S17 = Sesar et al. (2017); V17 = Vivas et al. (2017); B21 = Bhardwaj et al. (2021); C08 = Cáceres & Catelan (2008); and M06 = Marconi et al. (2006).

<sup>a</sup> Semitheoretical relations based on Equations (3) and (5); see Section 4.2 for more details.

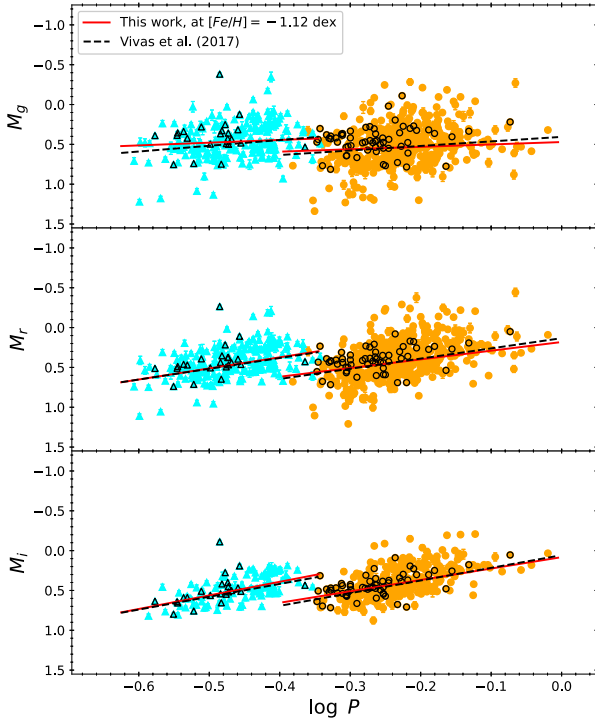


**Figure 17.** Comparison of the PL relations from Vivas et al. (2017; black dashed lines) and this work (i.e., Table 4; red solid lines) evaluated at  $[\text{Fe}/\text{H}] = -1.12$  dex for M5 (see Table 2). The orange circles and cyan triangles are for RR0 and RR1 in our sample, respectively. Data points with black circles or triangles represent the RR Lyrae in M5.

magnitudes of Vivas et al. (2017) from the DES system to the Pan-STARRS1 system. The averaged differences,  $\langle \text{Vivas}_{\text{PS1}} - \text{ZTF}_{\text{PS1}} \rangle$  (where  $\text{Vivas}_{\text{PS1}}$  are the transformed mean magnitudes, and  $\text{ZTF}_{\text{PS1}}$  are the ZTF mean magnitudes given in Table 3), were found to be small:  $-0.028$ ,  $-0.002$ , and  $+0.005$  mag (the corresponding standard deviations are 0.046, 0.052, and 0.060 mag) in the *gri* bands, respectively.

Finally, we compared our PL relations with the *gi*-band PL relations derived in Bhardwaj et al. (2021) using RR Lyrae in

the metal-poor globular cluster M15. Bhardwaj et al. (2021) calibrated their data in the SDSS photometric system, and the transformation between the SDSS and Pan-STARRS1 systems can be found in Tonry et al. (2012). Such a transformation, however, relies on the  $(g - r)$  colors, but the *r*-band data were absent in Bhardwaj et al. (2021). Therefore, we can only transform our data and PL relations to the SDSS photometric system. Furthermore, Bhardwaj et al. (2021) did not apply an absolute calibration to their PL relations; hence, we only compare the PL relations for RR Lyrae in M15. For  $\sim 60$  common RR Lyrae after transforming the mean magnitudes to the SDSS photometric system, the averaged difference in the *gi* bands is  $-0.023$  and  $0.023$  mag (with a corresponding standard deviation of 0.121 and 0.086 mag), respectively. The *gi*-band PL relation is compared in Figure 18 after transforming our mean magnitudes, as well as adding the correction term  $\delta_m$  (ranging from 0.046 to  $-0.003$  mag, applied separately to RR0, RR1, and the RR0+RR1 combined sample), and our PL relations to the SDSS photometric system. Overall, these two sets of PL relations nearly agree, although there is evidence that the zero-points of our *i*-band PL relations are slight fainter for RR1 and the RR0+RR1 combined sample.

#### 4.2. Comparisons to Published Results: Theoretical Relations

Two theoretical investigations of PLZ relations in the SDSS photometric system were presented in Marconi et al. (2006) and Cáceres & Catelan (2008). Metallicity in these theoretical investigations was expressed as  $\log Z$  instead of  $[\text{Fe}/\text{H}]$ . Therefore, a  $\log Z - [\text{Fe}/\text{H}]$  conversion was taken from Cáceres & Catelan (2008, and references therein) in the form of

$$\log Z = \log(0.638 \times 10^{[\alpha/\text{Fe}]} + 0.362) + [\text{Fe}/\text{H}] - 1.765. \quad (2)$$

For globular clusters,  $[\alpha/\text{Fe}]$  varies between  $\sim -0.1$  and  $\sim +0.5$  dex (based on the compilation presented in Pritzl et al. 2005). Therefore, we adopted  $[\alpha/\text{Fe}] = -0.1$  and  $+0.5$  dex, as well as the mid-point  $+0.2$  dex, to construct the theoretical PLZ relation.

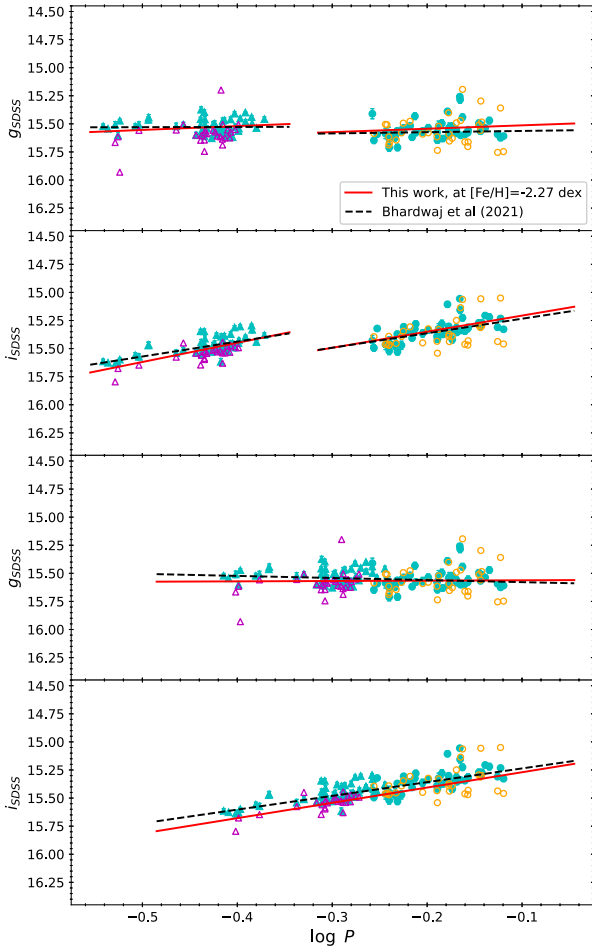


**Figure 18.** Comparison of the PL relations from Bhardwaj et al. (2021; black dashed lines) and this work (i.e., Table 4; red solid lines), evaluated at  $[\text{Fe}/\text{H}] = -2.27$  dex for M15 (see Table 2). The orange open circles and magenta open triangles are for RR0 and RR1 in our sample, respectively, with mean magnitudes transformed to the SDSS system. Filled light green circles and triangles represent the RR Lyrae taken from Bhardwaj et al. (2021). Consistent extinction of  $A_g = 0.379$  and  $A_i = 0.209$  (Bhardwaj et al. 2021) in the SDSS system was applied to all data points. Our PL relations were shifted vertically using the distance of M15 as listed in Table 2. The bottom two panels are for the combined sample of RR0 and RR1 after fundamentalizing the pulsation periods of RR1.

Cáceres & Catelan (2008) provided a simple  $i$ -band theoretical PLZ relation in the form of  $M_i = 0.908 - 1.035 \log P + 0.220 \log Z$ . This PLZ relation was compared to our derived PLZ relation in Figure 19 for the two adopted values of  $[\text{Fe}/\text{H}]$ . Figure 19 reveals that the slope of this theoretical  $i$ -band PLZ relation ( $-1.035$ ) is shallower than the one we derived here ( $-1.432 \pm 0.144$  for RR0 or  $-1.362 \pm 0.093$  for RR0+RR1) or the one derived in Vivas et al. (2017;  $-1.59 \pm 0.09$  for RR0). Furthermore, the predicted  $i$ -band absolute magnitudes, using the theoretical and our derived PLZ relations, show a moderate agreement for RR Lyrae with periods between  $\sim 0.5$  and  $\sim 0.6$  days at low metallicity (i.e.,  $[\text{Fe}/\text{H}] = -2.4$  dex). However, these two sets of PLZ relations are in disagreement when the metallicity is higher (as shown in the right panel of Figure 19 with  $[\text{Fe}/\text{H}] = -0.4$  dex) due to the difference in the zero-point ( $0.908$  versus  $-0.243 \pm 0.055$ ) and the metallicity term ( $0.220$  versus  $0.144 \pm 0.018$ ) of the  $i$ -band PLZ relations in both studies. Cáceres & Catelan (2008) cautioned the use of Equation (2) for

$Z > 0.003$  (VandenBerg et al. 2000), corresponding to  $[\text{Fe}/\text{H}] = -0.9$  dex (at  $[\alpha/\text{Fe}] = +0.2$  dex). This might contribute to the disagreement at high metallicity.

From Equation (2) and Figure 19, we note that the adopted value of  $[\alpha/\text{Fe}]$  only affects the zero-point of the PLZ relation. The difference in the PLZ zero-point between  $[\alpha/\text{Fe}] = -0.1$  and  $+0.2$  dex is  $c \times \Delta \log Z = -0.199c \sim \pm 0.044$  mag, and for  $[\alpha/\text{Fe}] = +0.2$  and  $+0.5$  dex, the difference is  $c \times \Delta \log Z = -0.239c \sim \pm 0.053$  mag at fixed  $[\text{Fe}/\text{H}]$ , where  $c = 0.220$  is the metallicity term in the theoretical  $i$ -band PLZ relation from Cáceres & Catelan (2008). Hence, we adopt a single value of  $[\alpha/\text{Fe}] = +0.2$  dex throughout the rest of the paper.

The theoretical PLZ relations derived in Marconi et al. (2006) are available in the  $ug$  bands, with additional terms on colors and masses. We can only compare our PLZ relations to their  $g$ -band PLZ relations, together with the  $(g-r)$  and  $(r-i)$  colors. We first realized that the slopes of the theoretical  $g$ -band PLZ relations (Marconi et al. 2006) are steep:  $-2.87$  and  $\sim -3.1$  for RR0 and RR1, respectively. These slopes are much steeper than those presented in Table 4 or Vivas et al. (2017). However, the Marconi et al. (2006) PLZ relations also included a color term, and the colors for RR Lyrae are expected to follow a PC relation (for example, see Section 5 and Cáceres & Catelan 2008 for colors in the  $gri$  bands). Combining the derived PCZ relations from Section 5 (see Table 4) with the theoretical PLZ relations from Marconi et al. (2006), we obtained the following semitheoretical PLZ relations<sup>21</sup> for RR0:

$$M_g = 0.066 - 0.311 \log P + 0.117[\text{Fe}/\text{H}] - 1.87 \log \frac{M}{M_\odot} - 0.06 \log Z + 3.35\delta_c \text{ [with } (g-r) \text{ color]}, \quad (3)$$

$$= -0.097 - 0.350 \log P - 0.003[\text{Fe}/\text{H}] - 1.94 \log \frac{M}{M_\odot} - 0.024 \log Z + 2.27\delta_c \text{ [with } (g-i) \text{ color]}. \quad (4)$$

The slopes of these semitheoretical relations are now closer to the empirical value given in Table 4 ( $-0.302 \pm 0.193$ ). Similarly, the semitheoretical PLZ relations for RR1 are

$$M_g = -0.109 - 0.322 \log P + 0.061[\text{Fe}/\text{H}] - 1.63 \log \frac{M}{M_\odot} - 0.042 \log Z + 3.57\delta_c \text{ [with } (g-r) \text{ color]}, \quad (5)$$

$$= 0.285 + 0.536 \log P + 0.033[\text{Fe}/\text{H}] - 1.72 \log \frac{M}{M_\odot} - 0.017 \log Z + 2.334\delta_c \text{ [with } (g-i) \text{ color]}. \quad (6)$$

The slope given in Equation (5) is closer to the empirical value of  $-0.342 \pm 0.289$ . However, the slope found in Equation (6) is drastically different; we do not have a formal explanation to account for this, perhaps due to a much steeper

<sup>21</sup> We intend to keep the two metallicity terms,  $[\text{Fe}/\text{H}]$  and  $\log Z$ , separate because  $[\text{Fe}/\text{H}]$  is taken from observations and  $\log Z$  is based on theoretical modelings, which in principle could follow a different  $\log Z$ - $[\text{Fe}/\text{H}]$  conversion, as given in Equation (2).

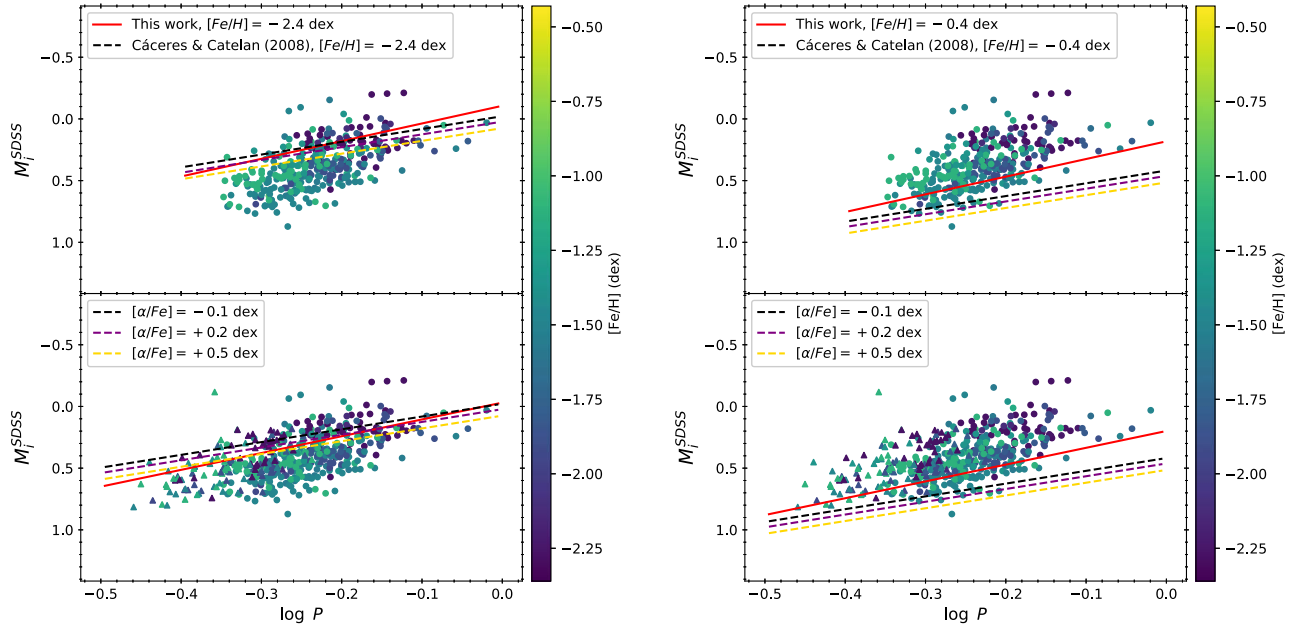


**Figure 19.** Comparison of the  $i$ -band PLZ relations given in Cáceres & Catelan (2008; dashed lines) and our derived relations presented in Table 4 (red solid lines), evaluated at  $[\text{Fe}/\text{H}] = -2.4$  (left panel) and  $-0.4$  (right panel) dex. For the theoretical PLZ relations, we also included the corresponding PLZ relations at three different adopted values of  $[\alpha/\text{Fe}]$  (see text for details). Note that the data points and our  $i$ -band PLZ relations have been transformed to the SDSS photometric system following the procedures described in Section 4.1. The top and bottom panels are for the RR0 only and RR0 and RR1 (after fundamentalizing the pulsation periods) combined samples, respectively.

slope for the RR1 ( $g-i$ ) PCZ relation.<sup>22</sup> We will adopt Equations (3) and (5) to compare to our derived PLZ relations because the slopes of these two semitheoretical relations are closer to the empirical values. The  $\delta_c$  in Equations (3)–(7) is the correction term to convert the colors from the Pan-STARRS1 photometric system to the SDSS photometric system, similar to the  $\delta_m$  described in Section 4.1. The comparison is presented in Figure 20.

An additional mass term,  $\log M/M_\odot$ , was included in Equations (3) and (5). Figure 20 reveals that this mass term has a larger impact on the zero-point of the PLZ relation, in contrast to the change of  $[\alpha/\text{Fe}]$  that affects the zero-point of the PLZ relation by a small amount ( $\lesssim 0.05$  mag). At a fixed metallicity, the  $g$ -band semitheoretical PLZ relations could be in agreement or disagreement with our derived  $g$ -band PLZ relations, depending on the adopted mass. For example, Figure 20 shows that at  $[\text{Fe}/\text{H}] = -2.4$  dex, these two sets of PLZ relations for RR0 agree when the mass is  $\sim 0.8 M_\odot$  but not for other lower masses. Similarly, at  $[\text{Fe}/\text{H}] = -0.4$  dex, the RR0 semitheoretical PLZ relations with mass of  $\sim 0.65 M_\odot$  are closer to the empirical PLZ relations given in Table 4.

## 5. The PCZ Relations and the Color–Color Diagram

We have fitted the extinction-corrected PCZ relations and the extinction-free period-Q-index-metallicity (PQZ) relation with our sample of RR Lyrae using Equation (1) and the same methodology as described in Section 4. The fitted results are summarized in Table 4 and shown in Figure 21. We note that the metallicity terms for the PCZ and PQZ relations, the

parameter  $c$  in Equation (1), are generally smaller than the PLZ and PWZ relations (except the  $W^{sr}$  PWZ relations; see Section 4). For example, the metallicity term in the ( $r-i$ ) PCZ relation for RR1 is consistent with zero. The ( $g-i$ ) PCZ relations have the steepest slopes and almost vanishing metallicity terms for either RR0, RR1, or the combined sample of both. Dispersions of the PCZ and PQZ relations are also smaller, with the ( $r-i$ ) PCZ relations have the smallest dispersion in all of the fitted relations.

Similar to the theoretical  $i$ -band PLZ relation, Cáceres & Catelan (2008) provided the theoretical PCZ relations in the ( $g-r$ ) and ( $r-i$ ) colors. We compared their PCZ relations with those listed in Table 4, evaluated at two metallicities, as shown in Figure 22. These theoretical PCZ relations behave similarly to the  $i$ -band PLZ relation (shown in Figure 19; see Section 4.2), such that they are in moderate agreement with our empirical relations at low metallicity and disagreement when the metallicity is high.

In addition to theoretical PLZ relations (see Section 4.2), Marconi et al. (2006) also derived the metallicity-dependent color–color relations based on a series of pulsation models. In Figure 23, these theoretical color–color relations are shown as solid and dashed lines for the two adopted metallicities (see Section 4.2 for more details), together with the extinction-corrected colors for our sample of RR Lyrae. It can be seen from Figure 23 that the theoretical color–color relations trace a relatively narrow “stripe” in the color–color diagram, while the observed RR Lyrae show a much larger scatter along this stripe. As discussed in Marconi et al. (2006), several sources (both intrinsic and observational), in addition to metallicity, may contribute to the scatter seen in the color–color relations. This implies that the ( $g-r$ ) and ( $r-i$ ) color–color diagram is not a good diagnostic to discriminate metallicity for RR Lyrae.

<sup>22</sup> To produce a slope of  $\sim -0.34$  for Equation (7), the slope for the RR1 ( $g-i$ ) PCZ relation would have to be  $\sim 1.17$ . The referee suggested using a relation of  $(g-i) = (g-r) + (r-i)$  to account for the slope of the ( $g-i$ ) PCZ relation. Using such a relation, the slope of Equation (7) would be reduced to 0.081, suggesting that there might be some problems associated with the  $i$ -band RR1 data.

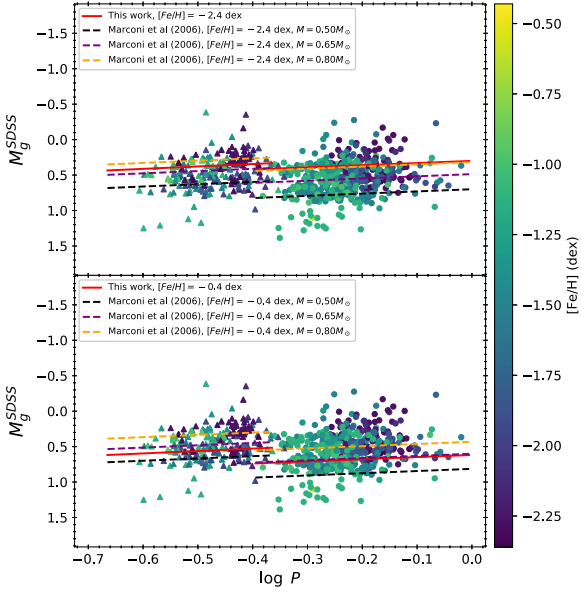


**Figure 20.** Comparison of the  $g$ -band PLZ relations given in Marconi et al. (2006; dashed lines) and our derived relations presented in Table 4 (red solid lines), evaluated at  $[\text{Fe}/\text{H}] = -2.4$  (top panel) and  $-0.4$  (bottom panel) dex, with a fixed  $[\alpha/\text{Fe}] = +0.2$  dex. For the semitheoretical PLZ relations (see text for details), we also included the corresponding PLZ relations at three different adopted values of the mass  $M$ , covering the expected mass range for RR Lyrae. Note that the data points and our  $g$ -band PLZ relations have been transformed to the SDSS photometric system following the procedures described in Section 4.1. Circles and triangles represent RR0 and RR1, respectively.

## 6. An Example of Application: Distance to Dwarf Galaxy Crater II

Based on DECam observations, Vivas et al. (2020) identified 83 and 5 RR0 and RR1, respectively, in the dwarf galaxy Crater II. There is one RR0 (V24, identified in Joo et al. 2018), however, missed in Vivas et al. (2020) because it is located outside the footprint of the DECam observations. This set of RR Lyrae provides an opportunity to compare and test various PL(Z) relations in a differential way. These include the empirical PL(Z) relations from Sesar et al. (2017), Vivas et al. (2017), and Bhardwaj et al. (2021; by adopting the distance to M15 as listed in Table 2) and our results presented in Table 4. We excluded the theoretical  $g$ -band PLZ relation from Marconi et al. (2006) because of the mass dependency, which has a significant impact on the zero-point of the PLZ relation (see discussion in Section 4.2). We also excluded the theoretical  $i$ -band PLZ relation from Cáceres & Catelan (2008) because Vivas et al. (2020) applied this relation to the RR Lyrae in Crater II and found a distance modulus of  $20.333 \pm 0.004$  mag to this dwarf galaxy by adopting  $[\text{Fe}/\text{H}] = -2.0$  and  $[\alpha/\text{Fe}] = +0.3$  dex.

Since the observed RR Lyrae are available in the SDSS  $gi$ -band (Vivas et al. 2020) and lack of  $r$ -band data, same as in the case of Bhardwaj et al. (2021), making the transformation between various photometric systems nontrivial. We first transformed our RR Lyrae in the globular clusters to the SDSS photometric system, and a subset of these RR Lyrae with the same mean  $(g-i)$  colors as the RR Lyrae in Crater II were used to determine the correction term,  $\delta_m$ , for the PLZ relations based on the Pan-STARRS1 photometric system. These correction terms were found to be 0.040 and 0.029 mag in the  $g$  band and  $-0.003$  and  $-0.004$  mag in the  $i$  band, where the first and second numbers are for RR0 and RR1,

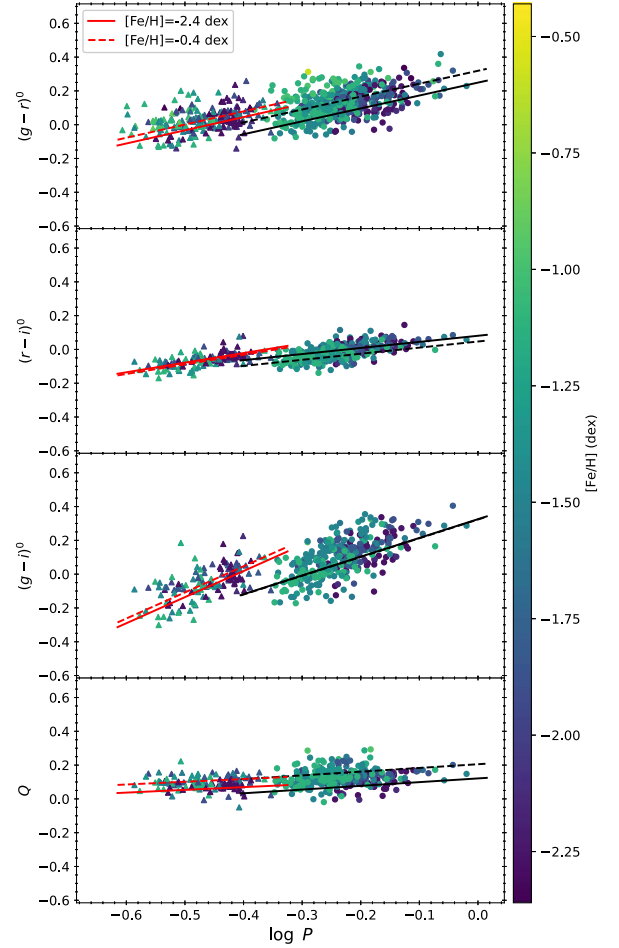


**Figure 21.** Extinction-corrected PC relations (top three panels) and extinction-free PQ relation (bottom panel) for our sample of RR Lyrae. The solid and dashed lines (in both red and black) represent the PCZ and PQZ relations evaluated at  $[\text{Fe}/\text{H}] = -2.4$  and  $-0.4$  dex, respectively. The relations for the combined sample of RR0 and RR1 (after fundamentalizing the periods) are similar; hence, they are not included in this figure.

respectively. In Table 6, we summarized the derived distance moduli ( $\mu$ ) using the four mentioned empirical PL(Z) relations at  $[\text{Fe}/\text{H}] = -2.0$  dex separately in the  $g$  and  $i$  bands while keeping the periods, mean magnitudes, and extinctions the same when fitting the PLZ relations to these RR Lyrae in Crater II.

Table 6 reveals that the derived distance moduli are generally larger than 20.333 mag, as determined in Vivas et al. (2020), except for the Sesar et al. (2017) PLZ relations and the  $i$ -band PL relations from Vivas et al. (2017). To bring the distance moduli fitted from other PL(Z) relations closer to 20.333 mag, the metallicity of Crater II has to increase. For the two sets of PL relations without the metallicity term, we note that the Bhardwaj et al. (2021) PL relations give a larger distance modulus than the PL relations derived in Vivas et al. (2017). The Bhardwaj et al. (2021) and Vivas et al. (2017) PL relations were derived using RR Lyrae in M15 and M5, respectively, where M15 is more metal-poor than M5; hence, the Bhardwaj et al. (2021) PL relations should be favored to be applied to RR Lyrae in Crater II (assuming its metallicity of  $[\text{Fe}/\text{H}] = -2.0$  dex is correct). Therefore, either the true distance modulus to Crater II is larger (than 20.333 mag), its metallicity is higher (than  $-2.0$  dex), or both.

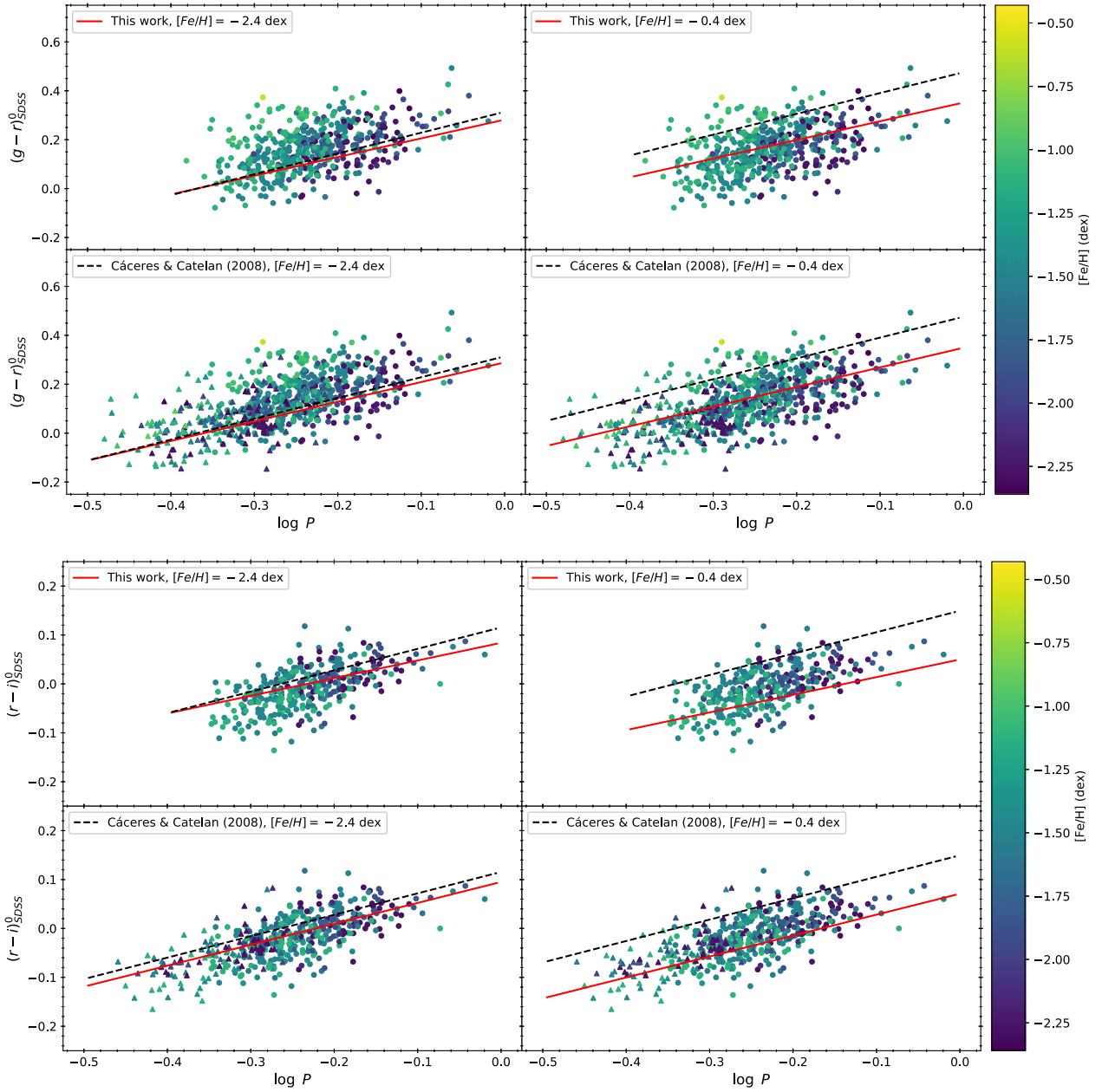


**Figure 22.** Comparison of the PCZ relations given in Cáceres & Catelan (2008; dashed lines) and our derived relations presented in Table 4 (red solid lines), evaluated at  $[Fe/H] = -2.4$  (left panels) and  $-0.4$  (right panels) dex, for the  $(g-r)$  and  $(r-i)$  colors in the top and bottom panels, respectively. For the theoretical PLZ relations, we adopted a value of  $[\alpha/Fe] = +0.2$  dex (see text for details). Note that the data points and our PCZ relations have been transformed to the SDSS photometric system following the procedures described in Section 4.1. In each panel, the top and bottom subpanels are for RR0 only and the RR0 and RR1 (after fundamentalizing the pulsation periods) combined samples, respectively.

Since the mean magnitudes have been corrected for extinction, we expect the  $g$ - and  $i$ -band distance moduli to be roughly the same, or  $\Delta\mu_{gi} = \mu_g - \mu_i \sim 0$ . Except for distance moduli fitted with the Sesar et al. (2017) PLZ relations (presumably due to the problem in the  $g$  band; see Section 4.1), we found that the  $g$ -band distance moduli are larger than their counterparts in the  $i$  band (Table 6). One possibility is the slightly incorrect estimation of extinction adopted in Vivas et al. (2017). Instead of using the  $E(B-V)$  values provided in Vivas et al. (2017), we use the same Bayerstar2019 3D reddening map as described in Section 2.2 to correct the extinction for the  $gi$ -band mean magnitudes. The fitted distance moduli are given in Table 7. Again, with the exception of distance moduli based on the Sesar et al. (2017) PLZ

relations, the  $gi$ -band distance moduli are now closer to each other. The Vivas et al. (2017) PL relations give the largest  $\Delta\mu_{gi}$ , indicating that an extra metallicity term must be applied to the derived distance moduli because the Vivas et al. (2017) PL relations are based on RR Lyrae in M5, which has a higher metallicity than the assumed metallicity for Crater II. We note that the  $\Delta\mu_{gi}$  from using our PLZ relations (Table 4) are larger than those using the PL relations from Bhardwaj et al. (2021), possibly due to the photometric transformation, because without the photometric transformation, the  $\Delta\mu_{gi}$  using our PLZ relations are even larger. Since, by definition, the difference of the distance moduli in two filters is also a measure of extinction (for example, see Kelson et al. 1996; Turner et al. 1998; Freedman et al. 2001),

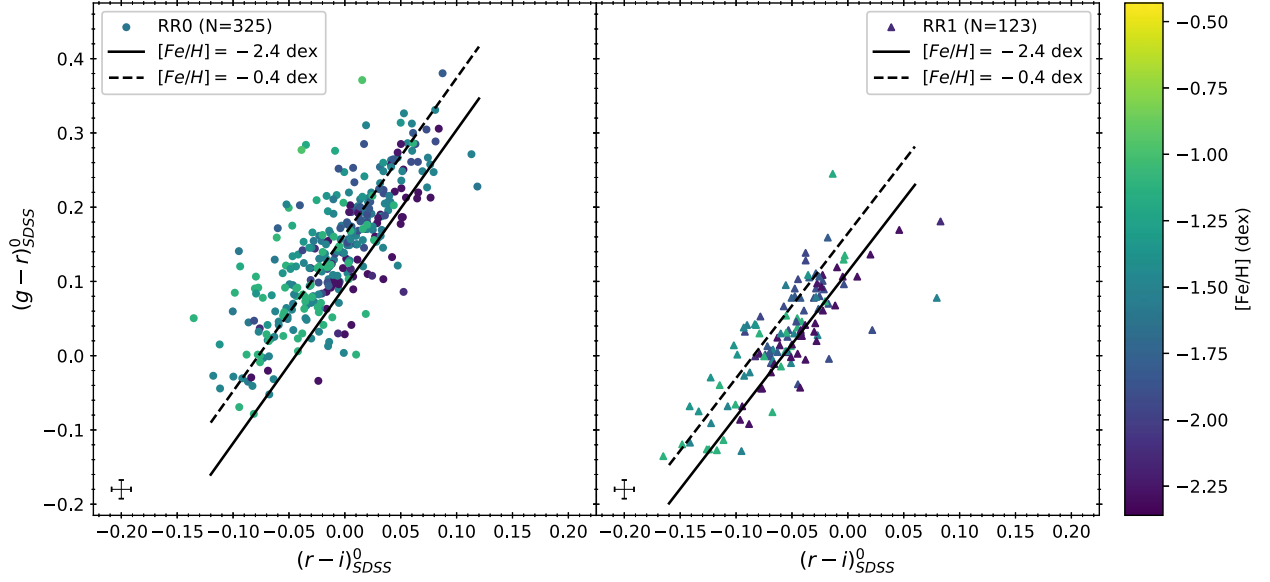


**Figure 23.** Extinction-corrected color–color relations for RR0 (left panel) and RR1 (right panel) in our sample, where the mean magnitudes have been transformed to the SDSS system using the transformations provided in Tonry et al. (2012). The typical error bars of the colors are shown in the lower left corners. Both the solid and dashed lines represent the theoretical color–color relations taken from Marconi et al. (2006) at a given metallicity (see text for more details).

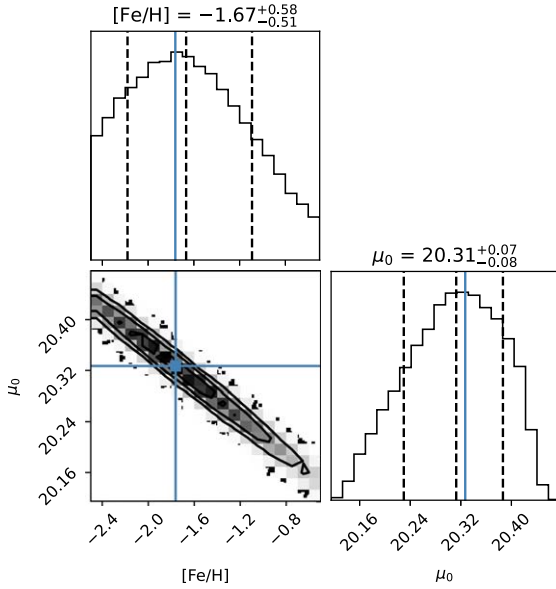


**Figure 24.** Corner plot based on the emcee sampling on the posterior distributions for  $\mu_0$  and  $[\text{Fe}/\text{H}]$ . The sampling was run with 128 walkers for 10,000 steps. The vertical dashed lines represent the 16th, 50th, and 84th percentiles of the distributions. The blue lines mark the results obtained from the OLS regression.

and the foreground extinctions have been corrected using the Bayerstar2019 3D reddening map, we suggest that the excess of  $\Delta\mu_{gi}$  is due to the internal extinction of Crater II, that is,  $\Delta_{gi} = (\mu_g + A_g) - (\mu_i + A_i) = E(g - i) \sim 0.03$  or  $\sim 0.01$  mag, depending on the adopted PL(Z) relations given in Table 4 or Bhardwaj et al. (2021).<sup>23</sup>

Since there should only be one distance modulus ( $\mu_0$ ) to Crater II, it is possible to simultaneously fit four PLZ relations, the  $gi$ -band PLZ relations for both RR0 and RR1, to the data by

defining the following merit function:

$$\chi^2 = \sum_{j=1}^{N_{\lambda,\psi}} \sum_{\lambda=\{g,i\}} \sum_{\psi=\{0,1\}} \frac{(m_{\lambda,\psi}^j - M_{\lambda,\psi}^j - \mu_0)^2}{\sigma_{\lambda,\psi}^2}$$

where  $M_{\lambda,\psi}^j = a_{\lambda,\psi} + b_{\lambda,\psi} \log P_{\lambda,\psi}^j + c_{\lambda,\psi} [\text{Fe}/\text{H}]$ . (7)

In the above equation,  $\lambda$  represents the filters (either  $g$  or  $i$ ), and  $\psi$  represents pulsation modes (either 0 or 1). Parameters  $a$ ,  $b$ , and  $c$  are the same as in the PLZ relation defined in Equation (1), and  $\sigma$  is the dispersion of the respected PLZ relation. Adopting  $[\text{Fe}/\text{H}] = -2.0$  dex and using the values given in Table 4 for our derived PLZ relations, we obtained  $\mu_0 = 20.361 \pm 0.004$  mag (random error only) after including the additional correction of internal extinction of Crater II,  $E(g - i) \sim 0.03$  mag, to the data. Allowing  $[\text{Fe}/\text{H}]$  as another free parameter to be fitted, we derived  $\mu_0 = 20.327 \pm 0.100$  mag and  $[\text{Fe}/\text{H}] = -1.76 \pm 0.69$  dex using the ordinary least-squares (OLS) regression. As a sanity check, we have also derived the distance modulus to Crater II using the  $W^{gi}$  PWZ relations, evaluated at  $[\text{Fe}/\text{H}] = -2.0$  dex. After transforming our PWZ relations to the SDSS photometric system and using  $W_{\text{SDSS}}^{gi} = g_{\text{SDSS}} - 2.058(g_{\text{SDSS}} - i_{\text{SDSS}})$ , we obtained  $\mu_0 = 20.354 \pm 0.004$  mag (random error only) by simultaneously fitting the RR0 and RR1 samples with Equation (7).<sup>24</sup> Since multiple transformations were involved for the Wesenheit index  $W^{gi}$ , we adopted our derived distance modulus based on the PLZ relations instead of the PWZ relations.

We recall that in general, a more metal-poor system would imply a larger distance modulus due to the positive metallicity term, the parameter  $c$  in Equation (1), in the PLZ relation. Our results are consistent with this expectation ( $\mu_0 = 20.361$  mag at  $[\text{Fe}/\text{H}] = -2.0$  dex versus  $\mu_0 = 20.327$  mag at  $[\text{Fe}/\text{H}] = -1.76$  dex). Clearly, there is a degeneracy, or correlation, between  $\mu_0$  and  $[\text{Fe}/\text{H}]$ . Therefore, instead of using OLS regression, we fit

<sup>23</sup> For comparison, the Bayerstar2019 interactive 3D reddening map returned a foreground extinction of  $E(g - r) = 0.06^{+0.02}_{-0.01}$  mag for Crater II.

<sup>24</sup> If only using the RR0 or RR1 sample, the resulting distance moduli are  $20.353 \pm 0.004$  and  $20.355 \pm 0.016$  mag (random error only), respectively, from the  $W^{gi}$  PWZ relations.

**Table 6**  
Distance Moduli to Crater II Derived with Various PL(Z) Relations Using  $[\text{Fe}/\text{H}] = -2.0$  dex

PLZ Relations	RR0			RR1			RR0+RR1		
	$\mu_g$	$\mu_i$	$\Delta\mu_{gi}$	$\mu_g$	$\mu_i$	$\Delta\mu_{gi}$	$\mu_g$	$\mu_i$	$\Delta\mu_{gi}$
This work (Table 4)	$20.488 \pm 0.006$	$20.427 \pm 0.004$	0.061	$20.465 \pm 0.016$	$20.406 \pm 0.014$	0.059	$20.450 \pm 0.006$	$20.375 \pm 0.004$	0.075
Vivas et al. (2017)	$20.374 \pm 0.006$	$20.277 \pm 0.005$	0.097	$20.396 \pm 0.017$	$20.287 \pm 0.014$	0.109	...	...	...
Sesar et al. (2017)	$20.262 \pm 0.008$	$20.287 \pm 0.005$	-0.025	...	...	...	...	...	...
Bhardwaj et al. (2021) <sup>a</sup>	$20.494 \pm 0.006$	$20.452 \pm 0.004$	0.042	$20.475 \pm 0.017$	$20.433 \pm 0.015$	0.042	$20.506 \pm 0.006$	$20.455 \pm 0.004$	0.051

**Note.** Here  $\Delta\mu_{gi} = \mu_g - \mu_i$  is the difference of the distance moduli in the  $g$  and  $i$  bands. Errors on each of the distance moduli are random errors only.

<sup>a</sup> Assuming the distance to M15 is 10.71 kpc, as listed in Table 2.

**Table 7**  
Same as Table 6 but with Reddening Values from the Bayerstar2019 3D Reddening Map

PLZ Relations	RR0			RR1			RR0+RR1		
	$\mu_g$	$\mu_i$	$\Delta\mu_{gi}$	$\mu_g$	$\mu_i$	$\Delta\mu_{gi}$	$\mu_g$	$\mu_i$	$\Delta\mu_{gi}$
This work (Table 4)	$20.426 \pm 0.007$	$20.395 \pm 0.005$	0.031	$20.393 \pm 0.016$	$20.369 \pm 0.012$	0.024	$20.387 \pm 0.007$	$20.343 \pm 0.005$	0.044
Vivas et al. (2017)	$20.312 \pm 0.008$	$20.245 \pm 0.005$	0.067	$20.325 \pm 0.014$	$20.250 \pm 0.013$	0.075	...	...	...
Sesar et al. (2017)	$20.200 \pm 0.009$	$20.255 \pm 0.005$	-0.055	...	...	...	...	...	...
Bhardwaj et al. (2021) <sup>a</sup>	$20.432 \pm 0.007$	$20.420 \pm 0.005$	0.012	$20.404 \pm 0.019$	$20.396 \pm 0.015$	0.008	$20.444 \pm 0.007$	$20.423 \pm 0.005$	0.021

**Note.** Here  $\Delta\mu_{gi} = \mu_g - \mu_i$  is the difference of the distance moduli in the  $g$  and  $i$  bands. Errors on each of the distance moduli are random errors only.

<sup>a</sup> Assuming the distance to M15 is 10.71 kpc, as listed in Table 2.

Equation (7) using the technique of Bayesian linear regression to the data. We adopted a flat (uniform) prior on both  $\mu_0$  (between 10 and 30) and  $[\text{Fe}/\text{H}]$  (between  $-2.5$  and  $-0.5$ ), and the affine-invariant Markov Chain Monte Carlo sampler package `emcee`<sup>25</sup> (Foreman-Mackey et al. 2013) was used to sample the posterior distribution. The result is shown in Figure 24, produced from the `corner` package<sup>26</sup> (Foreman-Mackey 2016), at which the (anti)correlation of these two parameters can be clearly seen. By adopting the median as the estimator of the parameters, we found the following best-fit values:  $\mu_0 = 20.313_{-0.083}^{+0.074}$  mag and  $[\text{Fe}/\text{H}] = -1.67_{-0.51}^{+0.58}$  dex, where the error bars represent the 16th and 84th percentiles of the distributions.

Nevertheless, the metallicity of Crater II has been measured to be around  $-2.0$  dex from multiple studies (Torrealba et al. 2016; Caldwell et al. 2017; Fu et al. 2019; Walker et al. 2019) and unlikely to have a higher metallicity around  $-1.7$  dex. Therefore, the true distance modulus of Crater II should be larger than 20.333 mag, as reported in Vivas et al. (2020).

## 7. Conclusion

In this work, we derived the  $gri$ -band PLZ and PWZ relations in the Pan-STARRS1 photometric system based on  $\sim 750$  RR Lyrae located in 46 globular clusters. These PLZ and PWZ relations were derived as homogeneously as possible, such as only using the light-curve data from ZTF, correcting the extinction using the same Bayerstar2019 3D reddening map, and adopting the same sources for the metallicity and distances from the GOTHAM survey and Baumgardt & Vasiliev (2021), respectively. Table 4 presents the fitted results for these PLZ

and PWZ relations. Other results obtained in this work are summarized as follows.

1. Based on our simulations, we found that the derived mean magnitudes may not be reliable or accurate with the template light-curve fitting approach when the light curve has a smaller number of data points. We recommend only fitting the observed light curves with 10 or more data points for deriving the mean magnitudes. We have also derived an empirical fitting equation to estimate the errors on the fitted mean magnitudes.
2. Given that blending is unavoidable for RR Lyrae located in globular clusters, we applied several selection criteria to exclude RR Lyrae that might be affected by blending, as well as other RR Lyrae with problematic light curves. These selection criteria utilized information based on amplitudes, amplitude ratios, colors, and/or residuals from the PL and PW relations. In the case of the PL/PW residuals, we found that there are indications that, for RR Lyrae with brighter mean magnitudes (than expected), they also tend to have smaller amplitudes, strongly indicating the presence of blending.
3. We notice that the  $W^{gr}$  PWZ relations exhibit very weak metallicity dependence, similar to the theoretical PW relations constructed in the  $BVR$  band (Marconi et al. 2015). We also notice that the PLZ and PWZ relations involving the  $i$  band show the smallest dispersions; therefore, increasing the  $i$ -band ZTF observations in the near future would be beneficial.
4. Compared to the literature PL(Z) relations, we found that our PLZ relations disagree with those presented in Sesar et al. (2017; especially in the  $g$  band) but are in very good agreement with the PL relations derived in

<sup>25</sup> <https://emcee.readthedocs.io/en/stable/>

<sup>26</sup> <https://corner.readthedocs.io/en/latest/>

- Vivas et al. (2017). In comparison to the Bhardwaj et al. (2021) *gi*-band PL relations, we found fairly good agreement, although our PL(Z) relations are fainter in the *i* band for the RR1 and RR0+RR1 samples.
- The theoretical *i*-band PLZ relation derived in Cáceres & Catelan (2008) was comparable to our derived PLZ relation at low metallicity ( $[Fe/H] = -2.4$  dex). However, disagreement was found for these two sets of *i*-band PLZ relations at high metallicity ( $[Fe/H] = -0.4$  dex), presumably due to invalid  $\log Z - [Fe/H]$  conversion at high metallicity.
  - The comparison to the theoretical PLZ relations presented in Marconi et al. (2006) was more complicated due to the inclusion of colors and mass terms in the theoretical relations. To eliminate the color term, we substituted our derived PCZ relations with the theoretical relations and obtained semitheoretical PLZ-mass relations. The mass term in these relations has a nonnegligible impact on the zero-point of the corresponding PLZ relation.
  - In addition to the PLZ and PWZ relations, we have also derived the PCZ and PQZ relations with our sample of RR Lyrae in globular clusters. Again, our empirical PCZ relations are in moderate agreement with the theoretical PCZ relations (Cáceres & Catelan 2008) at low metallicity but not high metallicity, probably for the same reason(s) as in the case of the *i*-band PLZ relation.
  - The empirical color-color diagram shows a larger scatter than the theoretical color-color relations at various metallicities. This implies that the  $(g-r)$  and  $(r-i)$  color-color diagram is not a good diagnostic for determining the metallicity for RR Lyrae.
  - We applied the empirical PL(Z) relations to RR Lyrae found in the dwarf galaxy Crater II. Using published data, we found that the derived distance modulus to Crater II is generally larger than 20.333 mag (Vivas et al. 2020). Further analysis revealed that Crater II needs to be more metal-rich in order to bring the distance modulus derived using our PLZ relations closer to the published values, or Crater II is indeed located at a further distance. Based on our analysis, we suggested that Crater II may have an internal extinction of  $E(g-i) \sim 0.01$  or  $\sim 0.03$  mag.

Our derived PLZ and PWZ relations in the *gri* bands would be beneficial for various distance scale applications. For example, a precise distance can be derived to faint RR Lyrae located in the outer Galactic halo or newly discovered (ultrafaint or diffuse) dwarf galaxies, such as those discovered from the HyperSuprime-Cam Subaru Strategic Program (HSC-SSP; Aihara et al. 2018) in the northern sky and the Vera Rubin Observatory Legacy Survey of Space and Time (LSST; Ivezić et al. 2019) in the southern sky, as well as other similar optical surveys. This, in turn, is of great interest for the study of substructure in our Galactic halo (for example, see Lancaster et al. 2019). At present, RR Lyrae observations are possible up to  $\sim 2$  Mpc distance (Da Costa et al. 2010), just slightly beyond the Local Group, and we anticipate that new dwarf galaxies will be routinely discovered in various optical surveys (such as HSC-SSP and/or LSST); an example is Eridanus IV, recently reported in Cerny et al. (2021).

We are thankful for the useful discussions and comments from an anonymous referee that improved the manuscript and from H. Baumgardt regarding the distance to the globular

clusters. We are thankful for funding from the Ministry of Science and Technology (Taiwan) under contracts 107-2119-M-008-014-MY2, 107-2119-M-008-012, 108-2628-M-007-005-RSP, and 109-2112-M-008-014-MY3.

Based on observations (prior to 2020 December 1) obtained with the Samuel Oschin Telescope 48 inch and the 60 inch Telescope at the Palomar Observatory as part of the Zwicky Transient Facility project. The ZTF is supported by the National Science Foundation under grant No. AST-1440341 and a collaboration including Caltech, IPAC, the Weizmann Institute for Science, the Oskar Klein Center at Stockholm University, the University of Maryland, the University of Washington, Deutsches Elektronen-Synchrotron and Humboldt University, Los Alamos National Laboratories, the TANGO Consortium of Taiwan, the University of Wisconsin at Milwaukee, and Lawrence Berkeley National Laboratory. Operations are conducted by COO, IPAC, and UW.

Based on observations (after 2020 December 1) obtained with the Samuel Oschin Telescope 48 inch and the 60 inch Telescope at the Palomar Observatory as part of the Zwicky Transient Facility project. The ZTF is supported by the National Science Foundation under grant No. AST-2034437 and a collaboration including Caltech, IPAC, the Weizmann Institute for Science, the Oskar Klein Center at Stockholm University, the University of Maryland, Deutsches Elektronen-Synchrotron and Humboldt University, the TANGO Consortium of Taiwan, the University of Wisconsin at Milwaukee, Trinity College Dublin, Lawrence Livermore National Laboratory, and IN2P3, France. Operations are conducted by COO, IPAC, and UW.

This research has made use of the SIMBAD database and the VizieR catalog access tool, operated at CDS, Strasbourg, France. This research made use of Astropy,<sup>27</sup> a community-developed core Python package for astronomy (Astropy Collaboration et al. 2013, 2018).

*Facility:* PO:1.2m.

*Software:* astropy (Astropy Collaboration et al. 2013, 2018), dustmaps (Green 2018), gatspy (VanderPlas and Ivezić 2015), Matplotlib (Hunter 2007), NumPy (Harris et al. 2020), SciPy (Virtanen et al. 2020), boundfit (Cardiel 2009), corner (Foreman-Mackey 2016), emcee (Foreman-Mackey et al. 2013).

## ORCID iDs

Chow-Choong Ngeow  <https://orcid.org/0000-0001-8771-7554>  
 Anupam Bhardwaj  <https://orcid.org/0000-0001-6147-3360>  
 Richard Dekany  <https://orcid.org/0000-0002-5884-7867>  
 Dmitry A. Duev  <https://orcid.org/0000-0001-5060-8733>  
 Matthew J. Graham  <https://orcid.org/0000-0002-3168-0139>  
 Steven L. Groom  <https://orcid.org/0000-0001-5668-3507>  
 Ashish A. Mahabal  <https://orcid.org/0000-0003-2242-0244>  
 Frank J. Masci  <https://orcid.org/0000-0002-8532-9395>  
 Michael S. Medford  <https://orcid.org/0000-0002-7226-0659>  
 Reed Riddle  <https://orcid.org/0000-0002-0387-370X>

## References

- Abbott, T. M. C., Adamów, M., Agüena, M., et al. 2021, *ApJS*, 255, 20  
 Aihara, H., Arimoto, N., Armstrong, R., et al. 2018, *PASJ*, 70, S4  
 Astropy Collaboration, Robitaille, T. P., Tollerud, E. J., et al. 2013, *A&A*, 558, A33

<sup>27</sup> <http://www.astropy.org>

- Astropy Collaboration, Price-Whelan, A. M., Sipőcz, B. M., et al. 2018, *AJ*, **156**, 123
- Baumgardt, H., & Vasiliev, E. 2021, *MNRAS*, **505**, 5957
- Beaton, R. L., Bono, G., Braga, V. F., et al. 2018, *SSRv*, **214**, 113
- Bellm, E., & Kulkarni, S. 2017, *NatAs*, **1**, 0071
- Bellm, E. C., Kulkarni, S. R., Graham, M. J., et al. 2019, *PASP*, **131**, 018002
- Benkő, J. M., Bakos, G. Á., & Nuspl, J. 2006, *MNRAS*, **372**, 1657
- Bhardwaj, A. 2020, *JApA*, **41**, 23
- Bhardwaj, A. B. 2022, *Univ*, **8**, 122
- Bhardwaj, A., Kanbur, S. M., Macri, L. M., et al. 2016, *AJ*, **151**, 88
- Bhardwaj, A., Rejkuba, M., de Grijs, R., et al. 2020, *AJ*, **160**, 220
- Bhardwaj, A., Rejkuba, M., Sloan, G. C., et al. 2021, *ApJ*, **922**, 20
- Bono, G. 2003, in *Stellar Candles for the Extragalactic*, Lecture Notes in Physics, ed. D. Alloin & W. Gieren, Vol. 635 (Berlin: Springer), **85**
- Bono, G., Caputo, F., Castellani, V., et al. 2001, *MNRAS*, **326**, 1183
- Bono, G., Caputo, F., Castellani, V., et al. 2003, *MNRAS*, **344**, 1097
- Bono, G., Braga, V. F., Pietrinferni, A., et al. 2016, *MmSAI*, **87**, 358
- Borissova, J., Ivanov, V. D., Stephens, A. W., et al. 2007, *A&A*, **474**, 121
- Braga, V. F., Stetson, P. B., Bono, G., et al. 2016, *AJ*, **152**, 170
- Caldwell, N., Walker, M. G., Mateo, M., et al. 2017, *ApJ*, **839**, 20
- Cardiel, N. 2009, *MNRAS*, **396**, 680
- Catelan, M., Pritzl, B. J., & Smith, H. A. 2004, *ApJS*, **154**, 633
- Cáceres, C., & Catelan, M. 2008, *ApJS*, **179**, 242
- Cerny, W., Pace, A. B., Drica-Wagner, A., et al. 2021, *ApJL*, **920**, L44
- Chambers, K. C., Magnier, E. A., Metcalfe, N., et al. 2016, arXiv:1612.05560
- Chicherov, A. V. 1997, *AstL*, **23**, 600
- Clement, C. M., Muzzin, A., Dufton, Q., et al. 2001, *AJ*, **122**, 2587
- Clement, C. M. 2017, *yCat*, **V/150**
- Coppola, G., Marconi, M., Stetson, P. B., et al. 2015, *ApJ*, **814**, 71
- Corwin, T. M., & Carney, B. W. 2001, *AJ*, **122**, 3183
- Da Costa, G. S., Rejkuba, M., Jerjen, H., et al. 2010, *ApJL*, **708**, L121
- Dambis, A. K., Rastorguev, A. S., & Zabolotskikh, M. V. 2014, *MNRAS*, **439**, 3765
- Dark Energy Survey Collaboration, Abbott, T., Abdalla, F. B., et al. 2016, *MNRAS*, **460**, 1270
- Dekany, R., Smith, R. M., Riddle, R., et al. 2020, *PASP*, **132**, 038001
- Dias, B., Barbuy, B., Saviane, I., et al. 2015, *A&A*, **573**, A13
- Dias, B., Barbuy, B., Saviane, I., et al. 2016a, *A&A*, **590**, A9
- Dias, B., Saviane, I., Barbuy, B., et al. 2016b, *Msngr*, **165**, 19
- Drake, A. J., Catelan, M., Djorgovski, S. G., et al. 2013, *ApJ*, **763**, 32
- Flaugher, B., Diehl, H. T., Honscheid, K., et al. 2015, *AJ*, **150**, 150
- Foreman-Mackey, D. 2016, *JOSS*, **1**, 24
- Foreman-Mackey, D., Hogg, D. W., Lang, D., et al. 2013, *PASP*, **125**, 306
- Freedman, W. L., Madore, B. F., Gibson, B. K., et al. 2001, *ApJ*, **553**, 47
- Fu, S. W., Simon, J. D., & Alarcón Jara, A. G. 2019, *ApJ*, **883**, 11
- Graham, M. J., Kulkarni, S. R., Bellm, E. C., et al. 2019, *PASP*, **131**, 078001
- Green, G. M. 2018, *JOSS*, **3**, 695
- Green, G. M., Schlafly, E., Zucker, C., et al. 2019, *ApJ*, **887**, 93
- Guhathakurta, P., Yanny, B., Bahcall, J. N., et al. 1994, *AJ*, **108**, 1786
- Harris, C. R., Millman, K. J., van der Walt, S. J., et al. 2020, *Natur*, **585**, 357
- Heinze, A. N., Tonry, J. L., Denneau, L., et al. 2018, *AJ*, **156**, 241
- Hunter, J. D. 2007, *CSE*, **9**, 90
- Iben, I. 1974, *ARA&A*, **12**, 215
- Ivezić, Ž., Kahn, S. M., Tyson, J. A., et al. 2019, *ApJ*, **873**, 111
- Joo, S.-J., Kyeong, J., Yang, S.-C., et al. 2018, *ApJ*, **861**, 23
- Kelson, D. D., Illingworth, G. D., Freedman, W. F., et al. 1996, *ApJ*, **463**, 26
- Kochanek, C. S., Shappee, B. J., Stanek, K. Z., et al. 2017, *PASP*, **129**, 104502
- Kopacki, G. 2013, *AcA*, **63**, 91
- Kunder, A., Stetson, P. B., Cassisi, S., et al. 2013, *AJ*, **146**, 119
- Lancaster, L., Belokurov, V., & Evans, N. W. 2019, *MNRAS*, **484**, 2556
- Madore, B. F. 1982, *ApJ*, **253**, 575
- Madore, B. F., & Freedman, W. L. 1991, *PASP*, **103**, 933
- Magnier, E. A., Sweeney, W. E., Chambers, K. C., et al. 2020, *ApJS*, **251**, 5
- Marconi, M., Caputo, F., Di Criscienzo, M., et al. 2003, *ApJ*, **596**, 299
- Marconi, M., Cignoni, M., Di Criscienzo, M., et al. 2006, *MNRAS*, **371**, 1503
- Marconi, M., Coppola, G., Bono, G., et al. 2015, *ApJ*, **808**, 50
- Masci, F. J., Laher, R. R., Rusholme, B., et al. 2019, *PASP*, **131**, 018003
- Muraveva, T., Delgado, H. E., Clementini, G., et al. 2018, *MNRAS*, **481**, 1195
- Neeley, J. R., Marengo, M., Bono, G., et al. 2017, *ApJ*, **841**, 84
- Neeley, J. R., Marengo, M., Freedman, W. L., et al. 2019, *MNRAS*, **490**, 4254
- Nemec, J. M., Nemec, A. F. L., & Lutz, T. E. 1994, *AJ*, **108**, 222
- Ngeow, C.-C., Liao, S.-H., Bellm, E. C., et al. 2021, *AJ*, **162**, 63
- Pollacco, D. L., Skillen, I., Collier Cameron, A., et al. 2006, *PASP*, **118**, 1407
- Pritzl, B. J., Venn, K. A., & Irwin, M. 2005, *AJ*, **130**, 2140
- Riess, A. G., Yuan, W., Casertano, S., et al. 2020, *ApJL*, **896**, L43
- Sandage, A., & Tammann, G. A. 2006, *ARA&A*, **44**, 93
- Sesar, B., Ivezić, Ž., Grammer, S. H., et al. 2010, *ApJ*, **708**, 717
- Sesar, B., Stuart, J. S., Ivezić, Ž., et al. 2011, *AJ*, **142**, 190
- Sesar, B., Hernitschek, N., Mitrović, S., et al. 2017, *AJ*, **153**, 204
- Smith, H. A. 2004, in *RR Lyrae Stars*, 2004 ed. H. A. Smith (Cambridge: Cambridge Univ. Press), **166**
- Sollima, A., Cacciari, C., & Valentini, E. 2006, *MNRAS*, **372**, 1675
- Tonry, J. L., Stubbs, C. W., Lykke, K. R., et al. 2012, *ApJ*, **750**, 99
- Tonry, J. L., Denneau, L., Heinze, A. N., et al. 2018, *PASP*, **130**, 064505
- Torreallba, G., Kuposov, S. E., Belokurov, V., et al. 2016, *MNRAS*, **459**, 2370
- Turner, A., Ferrarese, L., Saha, A., et al. 1998, *ApJ*, **505**, 207
- VandenBerg, D. A., Swenson, F. J., Rogers, F. J., et al. 2000, *ApJ*, **532**, 430
- VanderPlas, J. T., & Ivezić, Ž. 2015, *ApJ*, **812**, 18
- VanderPlas, J. 2016, *gatspy*: General tools for Astronomical Time Series in Python, Astrophysics Source Code Library, ascl:1610.007
- Vásquez, S., Saviane, I., Held, E. V., et al. 2018, *A&A*, **619**, A13
- Virtanen, P., Gommers, R., Oliphant, T. E., et al. 2020, *NatMe*, **17**, 261
- Vivas, A. K., Saha, A., Olsen, K., et al. 2017, *AJ*, **154**, 85
- Vivas, A. K., Walker, A. R., Martínez-Vázquez, C. E., et al. 2020, *MNRAS*, **492**, 1061
- Walker, A. R., Martínez-Vázquez, C. E., Monelli, M., et al. 2019, *MNRAS*, **490**, 4121